



On the self-similarity of unbounded viscous Marangoni flows

Fernando Temprano-Coletto^{1,2,†} and H.A. Stone^{2,†}

¹Andlinger Center for Energy and the Environment, Princeton University, Princeton, NJ 08544, USA

²Department of Mechanical and Aerospace Engineering, Princeton University, Princeton, NJ 08544, USA

(Received 24 January 2024; revised 17 July 2024; accepted 18 July 2024)

The Marangoni flow induced by an insoluble surfactant on a fluid–fluid interface is a fundamental problem investigated extensively due to its implications in colloid science, biology, the environment and industrial applications. Here, we study the limit of a deep liquid subphase with negligible inertia (low Reynolds number, $Re \ll 1$), where the two-dimensional problem has been shown to be described by the complex Burgers equation. We analyse the problem through a self-similar formulation, providing further insights into its structure and revealing its universal features. Six different similarity solutions are found. One of the solutions includes surfactant diffusion, whereas the other five, which are identified through a phase-plane formalism, hold only in the limit of negligible diffusion (high surface Péclet number $Pe_s \gg 1$). Surfactant ‘pulses’, with a locally higher concentration that spreads outward, lead to two similarity solutions of the first kind with a similarity exponent $\beta = 1/2$. On the other hand, distributions that are locally depleted and flow inwards lead to similarity of the second kind, with two different exponents that we obtain exactly using stability arguments. We distinguish between ‘dimple’ solutions, where the surfactant has a quadratic minimum and $\beta = 2$, from ‘hole’ solutions, where the concentration profile is flatter than quadratic and $\beta = 3/2$. Each of these two cases exhibits two similarity solutions, one valid prior to a critical time t_* when the derivative of the concentration is singular, and another one valid after t_* . We obtain all six solutions in closed form, and discuss predictions that can be extracted from these results.

Key words: multiphase flow

† Email addresses for correspondence: ftempranocoleto@princeton.edu, hastone@princeton.edu

© The Author(s), 2024. Published by Cambridge University Press. This is an Open Access article, distributed under the terms of the Creative Commons Attribution licence (<http://creativecommons.org/licenses/by/4.0>), which permits unrestricted re-use, distribution and reproduction, provided the original article is properly cited.

1. Introduction

When the interface between two fluids is laden with a non-uniform distribution of surfactant, the resulting imbalance of surface tension triggers a Marangoni flow (Scriven & Sternling 1960; de Gennes, Brochard-Wyart & Quéré 2004). The underlying dynamics is nonlinear, since the surfactant distribution, which sets the surface-driven fluid flow, is itself redistributed by the resulting velocity field through advection. This two-way coupled problem has been the focus of numerous studies, as surface-active molecules are virtually unavoidable in realistic multiphase flow problems, appearing both in natural and engineered systems (Manikantan & Squires 2020). For example, ambient amounts of surfactant are known to critically alter flows relevant to the environment like the motion of bubbles and drops, through a mechanism first proposed by Frumkin & Levich (1947) that has since been studied extensively (Griffith 1962; Schechter & Farley 1963; Wasserman & Slattery 1969; Sadhal & Johnson 1983; Cuenot, Magnaudet & Spennato 1997; Wang, Papageorgiou & Maldarelli 1999; Palaparthi, Papageorgiou & Maldarelli 2006, to name a few). Likewise, the surface of the ocean is affected by surfactants, which alter the dynamics of waves ranging from small capillary ripples (Lucassen & Van Den Tempel 1972; Alpers & Hühnerfuss 1989) to larger spilling and plunging breakers (Liu & Duncan 2003; Erinin *et al.* 2023). Marangoni flows also play an important role in biological fluid mechanics, both in physiological transport processes within the lung (Grotberg, Halpern & Jensen 1995) or the ocular globe (Zhong *et al.* 2019), and in the motion of colonies of microorganisms that generate biosurfactants (Botte & Mansutti 2005; Trinschek, John & Thiele 2018). In industrially relevant applications, it is well known that surface-active molecules influence the dip coating of plates and fibres (Park 1991; Quéré 1999), the drag reduction of superhydrophobic surfaces (Peaudecerf *et al.* 2017; Song *et al.* 2018; Temprano-Coleto *et al.* 2023) or the stability of foams (Breward & Howell 2002; Cantat *et al.* 2013).

One of the most fundamentally important examples of flows induced by surfactants is the so-called ‘Marangoni spreading’ (Matar & Craster 2009), where a locally concentrated surfactant spreads unopposed on a clean interface until it reaches a uniform equilibrium concentration. Early quantitative studies examined surfactant spreading on thin films, due to their relevance in pulmonary flows (Ahmad & Hansen 1972; Borgas & Grotberg 1988; Gaver & Grotberg 1990, 1992). The pioneering work of Jensen & Grotberg (1992) investigated the spreading of insoluble surfactant from the perspective of self-similarity, a powerful theoretical tool to identify universal, scale-free behaviour in physical systems (Barenblatt 1996). Several studies of Marangoni flows on thin films based on self-similarity have since followed. For example, Jensen & Grotberg (1993) described the spreading of a soluble surfactant, while Jensen (1994) re-examined the insoluble case, finding additional self-similar solutions for distributions that are not locally concentrated, but depleted of surfactant, which flow inward (‘fill’) under the action of Marangoni stresses. Self-similarity was also examined for a deep fluid subphase by Jensen (1995), considering the limit of dominant fluid inertia (i.e. at high Reynolds number).

In all the above studies, the problem is simplified by the existence of a confining length scale in the fluid subphase, either the thickness of the thin liquid film or the width of the momentum boundary layer. Thess, Spirn & Jüttner (1995) considered the case of a deep fluid subphase at low Reynolds number, where the fluid flow is unconfined, and identified that the resulting problem is non-local, with the velocity field at any given position depending on the surfactant distribution on the whole interface. Theoretical work in this limit followed (Thess 1996; Thess, Spirn & Jüttner 1997) until, recently, Crowdy (2021b) showed that the problem is equivalent to a complex version of the Burgers equation

for a lower-analytic function, effectively providing a local reformulation using complex variables. This connection between the non-local problem and the Burgers equation had also been identified previously (Baker, Li & Morlet 1996; Chae *et al.* 2005; de la Hoz & Fontelos 2008), albeit in a context unrelated to surfactants or interfacial fluid dynamics. Applied to Marangoni flows, the complex variables formulation has been a key insight to derive new exact solutions (Crowdy 2021*b*; Bickel & Detcheverry 2022) and investigate extensions of the problem (Crowdy 2021*a*; Crowdy, Curran & Papageorgiou 2023).

Even after this simplification for low-Reynolds-number, deep-subphase Marangoni flow, exact solutions to the Burgers equation can be written explicitly only for a selected subset of initial conditions, limiting the generality of the resulting physical insights. In this paper, we analyse the problem from the perspective of self-similarity, which has provided key physical insights not only into Marangoni spreading, but into many other problems like boundary layer theory (Leal 2007), liquid film spreading (e.g. Huppert 1982; Brenner & Bertozzi 1993; Wu, Duprat & Stone 2024), drop coalescence (Kaneelil *et al.* 2022) and capillary pinching (Eggers 1993; Brenner, Lister & Stone 1996; Day, Hinch & Lister 1998). We show that self-similarity not only reveals new universal features about the problem that are independent of the specific initial conditions, but also gives rise to a beautiful mathematical structure with six different similarity solutions and three different rational exponents, all of which can be obtained in closed form.

We present the general formulation of the problem in § 2. Section 3 analyses the case of advection-dominated Marangoni flows, that is, in the limit of infinite surface Péclet number $Pe_s^{-1} = 0$. In particular, the different possible similarity solutions for this limit are identified through a combination of a phase-plane formalism (§ 3.1) and stability analysis (§ 3.2). In § 4, we consider the case of ‘spreading’, where locally concentrated surfactant induces an outward flow, and derive one solution without diffusion (§ 4.1) and one with diffusion (§ 4.2). Section 5 analyses locally depleted surfactant distributions, which induce a ‘filling’ flow inwards. Depending on the initial conditions, we distinguish that the filling dynamics converges to either ‘dimple’ (§ 5.1) or ‘hole’ (§ 5.2) solutions. For either case, we derive one similarity solution that holds prior to a reference time t_* where the derivative of the solution has a singularity, and another similarity solution valid after t_* . We discuss these results and draw conclusions in § 6.

2. Problem formulation

2.1. Governing equations

We consider the dynamics of an insoluble surfactant evolving on the free surface of a layer of incompressible, Newtonian fluid of density ρ and dynamic viscosity μ . Our focus is the limit of small Reynolds (Re) and capillary (Ca) numbers given by

$$Re = \frac{\rho u_c l_c}{\mu} \ll 1, \quad Ca = \frac{\mu u_c}{\gamma_0} \ll 1, \quad (2.1a,b)$$

where γ_0 is the surface tension of the clean (surfactant-free) interface, and l_c and u_c are the characteristic length and velocity scales of the problem, respectively. In this asymptotic limit, surface tension dominates over viscous stresses, keeping the interface flat. In addition, fluid inertia is negligible and the velocity field $\mathbf{u}(\mathbf{x}, t)$, which depends on both time t and position \mathbf{x} , is well described by the continuity and Stokes equations

$$\nabla \cdot \mathbf{u} = 0, \quad \nabla \cdot \boldsymbol{\sigma} = \mathbf{0}, \quad (2.2a,b)$$

where $\boldsymbol{\sigma}$ is the second-order stress tensor, $\boldsymbol{\sigma} = -p\mathbf{I} + \mu(\nabla\mathbf{u} + (\nabla\mathbf{u})^T)$, p the mechanical pressure and \mathbf{I} the identity tensor.

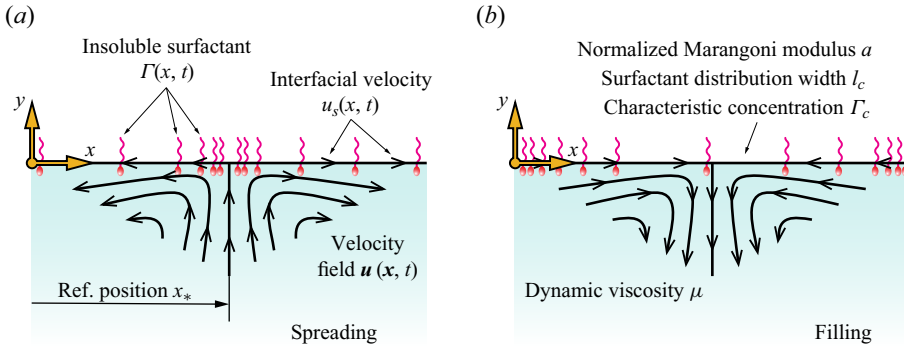


Figure 1. A non-homogeneous distribution of insoluble surfactant, with concentration $\Gamma(x, t)$, induces a velocity field $\mathbf{u}(x, t)$ within its fluid subphase through interfacial Marangoni stresses. The surfactant is itself advected by the resulting interfacial velocity $u_s(x, t) = \mathbf{u} \cdot \mathbf{e}_x|_{y=0}$, leading to a two-way coupled problem. (a) For a localized pulse of surfactant, the Marangoni flow results in outward ‘spreading’. (b) When the surfactant distribution is instead depleted at its centre (a ‘hole’ or a ‘dimple’), the result is an inward ‘filling’ flow. All the dimensional parameters of the model considered here are highlighted in panel (b).

For sufficiently elongated surfactant distributions (e.g. a ‘strip’ of surfactant) and a sufficiently deep fluid subphase, the problem can be reduced to the unbounded, two-dimensional scenario displayed in figure 1. We use a coordinate system where x spans the interface and y points away from the fluid subphase, with \mathbf{e}_x and \mathbf{e}_y the unit vectors in the x and y directions, respectively. Velocity components are denoted u and v , with $\mathbf{u} = u\mathbf{e}_x + v\mathbf{e}_y$. The domain is considered to be semi-infinite, defined in $x \in (-\infty, \infty)$ and $y \in (-\infty, 0]$, and the time evolution of the surfactant concentration $\Gamma(x, t)$ along the interface is given by

$$\frac{\partial \Gamma}{\partial t} + \frac{\partial (u_s \Gamma)}{\partial x} = D_s \frac{\partial^2 \Gamma}{\partial x^2}, \tag{2.3}$$

where D_s is the surface diffusivity of the surfactant and $u_s = \mathbf{u} \cdot \mathbf{e}_x|_{y=0}$ is the interfacial velocity. The boundary conditions at the interface

$$\mathbf{e}_x \cdot \boldsymbol{\sigma} \cdot \mathbf{e}_y|_{y=0} = -a \frac{\partial \Gamma}{\partial x}, \tag{2.4a}$$

$$v(y = 0) = 0, \tag{2.4b}$$

are the Marangoni condition (2.4a) linking viscous stresses to the gradient of surfactant, and the no-penetration kinematic condition (2.4b). Here, the parameter

$$a = \left| \frac{d\gamma}{d\Gamma} \right|, \tag{2.5}$$

is a normalized Marangoni modulus, quantifying the reduction of surface tension γ with increasing surfactant concentration. We regard D_s and a as constants, although they are in general dependent on Γ through equations of state $D_s(\Gamma)$ and $\gamma(\Gamma)$, e.g. see Manikantan & Squires (2020).

The governing equations (2.2)–(2.3) and boundary conditions (2.4) are supplemented with an initial condition for the surfactant distribution

$$\Gamma(x, t = 0) = \Gamma_0(x). \tag{2.6}$$

Self-similarity in unbounded viscous Marangoni flows

The profile $\Gamma_0(x)$ introduces the characteristic scale Γ_c , which we will take as the maximum concentration $\Gamma_c = \max_x [\Gamma_0(x)]$. Furthermore, the typical width of $\Gamma_0(x)$ sets the length scale l_c of the problem.

From these constants, dimensional analysis of the Marangoni boundary condition (2.4a) leads to a natural scale for the velocity magnitude

$$\mathbf{e}_x \cdot \boldsymbol{\sigma} \cdot \mathbf{e}_y|_{y=0} = \mu \frac{\partial u}{\partial y} \Big|_{y=0} = -a \frac{\partial \Gamma}{\partial x} \implies u_c \approx \frac{a\Gamma_c}{\mu}. \quad (2.7)$$

For the assumptions of $Re \ll 1$ and $Ca \ll 1$ to hold, the characteristic concentration Γ_c and width l_c of the surfactant distribution must both be sufficiently small to ensure that

$$l_c \Gamma_c \ll \frac{\mu^2}{\rho a}, \quad \Gamma_c \ll \frac{\gamma_0}{a}, \quad (2.8)$$

providing practical estimates to determine if, for a given set of physicochemical properties μ , ρ , a , and γ_0 , a known surfactant distribution will lead to Marangoni flow in the asymptotic limit considered in this study.

The full problem, as defined by (2.2)–(2.4) and (2.6), is nonlinear and involves the two-dimensional vector field \mathbf{u} . Thess *et al.* (1995) recognized that it was possible to obtain a one-dimensional formulation, using the Fourier transform of (2.2) to obtain u_s as a function of Γ . Here, we show that the same simplification can be achieved through the boundary integral representation of Stokes flow. Indeed, the velocity field given by (2.2) at any position \mathbf{x} along the interface (see Pozrikidis 1992) can be expressed as

$$\mathbf{u}(\mathbf{x}, t) = \frac{1}{2\pi} \left[\int_{\mathcal{I}} \mathbf{G}(\mathbf{x} - \mathbf{x}') \cdot \boldsymbol{\sigma}(\mathbf{x}', t) \cdot \mathbf{n} \, dl_{x'} + \int_{\mathcal{I}} \mathbf{u}(\mathbf{x}', t) \cdot \mathbf{T}(\mathbf{x} - \mathbf{x}') \cdot \mathbf{n} \, dl_{x'} \right], \quad (2.9)$$

where the dash denotes the Cauchy principal value of the integral, \mathcal{I} denotes the interface, \mathbf{n} the unit outward normal vector and the tensors in the integrands are defined as

$$\mathbf{G}(\mathbf{x}) = -\frac{1}{\mu} \left(\ln |\mathbf{x}| \mathbf{I} - \frac{\mathbf{x}\mathbf{x}}{|\mathbf{x}|^2} \right), \quad (2.10a)$$

$$\mathbf{T}(\mathbf{x}) = -4 \frac{\mathbf{x}\mathbf{x}\mathbf{x}}{|\mathbf{x}|^4}. \quad (2.10b)$$

Since the interface remains flat, the outward normal vector simplifies as $\mathbf{n} = \mathbf{e}_y$, while \mathbf{x} and \mathbf{x}' are co-linear and parallel to \mathbf{e}_x . Therefore, we have $(\mathbf{x} - \mathbf{x}') \cdot \mathbf{n} = 0$ since the vectors are orthogonal, and

$$\mathbf{T}(\mathbf{x} - \mathbf{x}') \cdot \mathbf{n} = -4 \frac{(\mathbf{x} - \mathbf{x}')(\mathbf{x} - \mathbf{x}')(\mathbf{x} - \mathbf{x}')}{|\mathbf{x} - \mathbf{x}'|^4} \cdot \mathbf{n} = \mathbf{0}, \quad (2.11)$$

eliminating the second integral (the ‘double-layer potential’) in (2.9). Taking $(\mathbf{x} - \mathbf{x}') = (\mathbf{x} - \mathbf{x}')\mathbf{e}_x$ and noting the integrals along the interface are simply along x' , the interfacial

velocity can then be expressed as

$$u_s(x, t) = \mathbf{e}_x \cdot \mathbf{u}|_{y=0} = \frac{1}{2\pi\mu} \int_{-\infty}^{\infty} (1 - \ln|x - x'|) \mathbf{e}_x \cdot \boldsymbol{\sigma}(x', t) \cdot \mathbf{e}_y|_{y=0} dx', \quad (2.12)$$

which, upon substitution of the Marangoni boundary condition (2.4a) and integration by parts, becomes

$$u_s(x, t) = \frac{a}{2\pi\mu} \left\{ [(\ln|x - x'| - 1) \Gamma(x', t)]_{x' \rightarrow -\infty}^{x' \rightarrow \infty} + \int_{-\infty}^{\infty} \frac{\Gamma(x', t)}{x - x'} dx' \right\}. \quad (2.13)$$

The first term in (2.13) vanishes for any surfactant profile decaying as a power law (or faster) in the far field. Remarkably, this term also cancels out for profiles $\Gamma(x, t)$ that do not decay as $|x| \rightarrow \infty$, as long as their far-field values are finite and symmetric, such that $0 < \lim_{x \rightarrow \infty} \Gamma(x, t) = \lim_{x \rightarrow -\infty} \Gamma(x, t) < \infty$. We therefore restrict this study to these two possible far-field behaviours, excluding ‘step-like’ profiles with asymmetric far-field concentrations. The above leads to the closure relationship

$$u_s(x, t) = \frac{a}{2\pi\mu} \int_{-\infty}^{\infty} \frac{\Gamma(x', t)}{x - x'} dx' = \frac{a}{2\mu} \mathcal{H}[\Gamma], \quad (2.14)$$

first derived by Thess *et al.* (1995), where the operator $\mathcal{H}[\]$ denotes the Hilbert transform of a function (for details, see King 2009a,b). This closure relationship results in a one-dimensional problem, only requiring the solution of (2.3) alongside condition (2.14). The resulting formulation is, however, non-local, as the interfacial velocity u_s at any given point depends upon the distribution of Γ along the whole real line.

We proceed to non-dimensionalize equations (2.3), (2.14) and the initial condition (2.6) using the scales of the problem discussed above. To that end, we apply the rescalings

$$x \rightarrow l_c x, \quad t \rightarrow \left(\frac{2\mu l_c}{a\Gamma_c}\right) t, \quad u \rightarrow \left(\frac{a\Gamma_c}{2\mu}\right) u, \quad \Gamma \rightarrow \Gamma_c \Gamma, \quad \Gamma_0 \rightarrow \Gamma_c \Gamma_0, \quad (2.15)$$

which leads to a dimensionless problem given by

$$\frac{\partial \Gamma}{\partial t} + \frac{\partial (\mathcal{H}[\Gamma] \Gamma)}{\partial x} = \frac{1}{Pe_s} \frac{\partial^2 \Gamma}{\partial x^2}, \quad (2.16a)$$

$$\Gamma(x, t = 0) = \Gamma_0(x), \quad (2.16b)$$

and where the surface Péclet number is defined as

$$Pe_s := \frac{a\Gamma_c l_c}{2\mu D_s}. \quad (2.17)$$

Alternative formulations of the non-local problem (2.16) have been studied in the mathematical literature (Baker *et al.* 1996; Morlet 1998; Chae *et al.* 2005; de la Hoz & Fontelos 2008; Eggers & Fontelos 2020) as a model for finite-time blowup. However, that body of work was not concerned with the description of surfactant dynamics, which introduces key differences that we highlight in § 2.3 below. In the context of Marangoni flows, Crowdy (2021b) recently showed, through a complex-variable formulation of two-dimensional Stokes flow, that a dependent variable

$\psi = u_s + i\Gamma = \mathcal{H}[\Gamma] + i\Gamma$ satisfies

$$\frac{\partial \psi}{\partial t} + \psi \frac{\partial \psi}{\partial x} = \frac{1}{Pe_s} \frac{\partial^2 \psi}{\partial x^2}, \tag{2.18a}$$

$$\psi(x, t = 0) = \psi_0(x) = \mathcal{H}[\Gamma_0(x)] + i\Gamma_0(x), \tag{2.18b}$$

where $\psi(z, t)$ must be a lower-analytic complex function (named $h(z, t)$ in the notation of Crowdy 2021b) of the variable $z = x + iy$. This problem reduction can also be realized by adding (2.16a) to its Hilbert transform, and then recognizing that $\mathcal{H}[\partial_x \Gamma] = \partial_x \mathcal{H}[\Gamma]$ and $\mathcal{H}[\Gamma \mathcal{H}[\Gamma]] = ((\mathcal{H}[\Gamma])^2 - \Gamma^2)/2$. It is worth remarking that subtracting (2.16a) from its Hilbert transform leads to the same Burgers equation (2.18a) but with a complex conjugate dependent variable $\psi = u_s - i\Gamma$, which is an equivalent notation followed by Bickel & Detcheverry (2022). In such an alternative notation the complex function $\psi(z, t)$ is instead the upper-analytic Schwarz conjugate of the one used here.

The limit of negligible diffusion given by $Pe_s \gg 1$ can be approximated at leading order by taking $Pe_s^{-1} = 0$, which yields

$$\frac{\partial \psi}{\partial t} + \psi \frac{\partial \psi}{\partial x} = 0, \tag{2.19a}$$

$$\psi(x, t = 0) = \psi_0(x) = \mathcal{H}[\Gamma_0(x)] + i\Gamma_0(x). \tag{2.19b}$$

The problems given by the Burgers equation (2.18a) and the inviscid Burgers equation (2.19a) (also known as the Hopf equation) are now local, and admit exact solutions via either the Cole–Hopf transformation for (2.18) or the method of characteristics for (2.19), as shown in Crowdy (2021b) and Bickel & Detcheverry (2022). While some of these solutions have been shown to exhibit self-similar behaviour (Thess 1996; Bickel & Detcheverry 2022), a systematic analysis of the problem from the perspective of self-similarity has not yet been performed, and is the goal of this paper.

2.2. Self-similar formulation

We adopt the following self-similarity ansatzes:

$$\eta = \text{sgn}(t - t_*) \frac{x - x_*}{A|t - t_*|^\beta}, \tag{2.20a}$$

$$\psi(x, t) = B|t - t_*|^\alpha f(\eta), \tag{2.20b}$$

with η the real similarity variable. The similarity function $f(\eta)$, which takes complex values, is decomposed as $f = U + iC$, with $U(\eta)$ and $C(\eta)$ real. The interfacial velocity and surfactant concentration can then be recovered as

$$u_s(x, t) = B|t - t_*|^\alpha U(\eta), \tag{2.21a}$$

$$\Gamma(x, t) = B|t - t_*|^\alpha C(\eta). \tag{2.21b}$$

We introduce the positive real constants A and B for convenience, and fix their values to simplify the final form of the similarity solutions $f(\eta)$, as illustrated below. The real constants x_* and t_* are a reference position and time, respectively. Including the factor

$\text{sgn}(t - t_*)$ in the definition (2.20a) is equivalent to choosing

$$\eta = \frac{x - x_*}{A(t - t_*)^\beta}, \tag{2.22a}$$

for solutions that evolve forward in time $t > t_*$, and to choosing

$$\eta = \frac{x_* - x}{A(t_* - t)^\beta}, \tag{2.22b}$$

for solutions that evolve backward in time $t < t_*$. We adopt the more intuitive forward-time description when describing ‘spreading’ (as in figure 1a) solutions of (2.18) and (2.19). These solutions become self-similar at long times $t \gg 1$, so in that case we take $t_* = 0$. However, ‘filling’ self-similar solutions representing inward flow (as in figure 1b) are often only valid sufficiently close to a reference time $t = t_* > 0$ at which the solution has a singularity, requiring either the backward-time (e.g. Eggers & Fontelos 2008) or the forward-time (e.g. Zheng *et al.* 2018) description to analyse their behaviour immediately prior or subsequent to t_* , respectively.

Using the self-similarity ansatzes (2.20) in the Burgers equation (2.18a) leads to

$$\alpha f - \beta \eta \frac{df}{d\eta} + \frac{B}{A} |t - t_*|^{\alpha - \beta + 1} f \frac{df}{d\eta} = \frac{\text{sgn}(t - t_*)}{A^2 Pe_s} |t - t_*|^{1 - 2\beta} \frac{d^2 f}{d\eta^2}. \tag{2.23}$$

Solutions are self-similar when the above ordinary differential equation (ODE) is solely dependent on η , and not on t or x separately, which requires either one of the following two scenarios:

- (i) For the general case of a finite $Pe_s^{-1} > 0$, the only possible choice of exponents is $\alpha = -1/2$, $\beta = 1/2$. Seeking to eliminate parameters from (2.23), we fix $A = B = \sqrt{2/Pe_s}$, focusing on forward-time solutions with $\text{sgn}(t - t_*) = 1$ that lead to

$$\frac{d}{d\eta} \left[\frac{df}{d\eta} + \eta f - f^2 \right] = 0. \tag{2.24}$$

Equation (2.24) has one spreading (as in figure 1a) self-similar solution of the first kind, which was identified by Bickel & Detchevry (2022) and which we outline in § 4.2.

- (ii) In the advection-dominated limit given by $Pe_s^{-1} = 0$, self-similarity only requires $\alpha = \beta - 1$. In this case, we fix $B = A$, keeping β and A as free parameters. This leads to

$$(f - \beta \eta) \frac{df}{d\eta} = (1 - \beta) f. \tag{2.25}$$

We obtain the same similarity equation (2.25) independently of the choice of the forward-time or backward-time definition of η , due to the invariance of the inviscid Burgers equation (2.19a) with respect to a reversal of time $t \rightarrow -t$ and space $x \rightarrow -x$. In this advection-dominated case, multiple solutions can potentially arise, depending on the specific value of β . Using a phase-plane formalism and stability analysis, in § 3 we identify five possible similarity solutions of (2.25). We re-discover the spreading self-similar solution of the first kind first identified by Thess (1996), which we detail in § 4.1. We also find four possible ‘filling’ (as in figure 1b) solutions of the second kind with different power-law exponents β , which we describe in § 5.

For either of the two similarity differential equations (2.24) and (2.25) above, solutions $f(\eta)$ must have a physically correct parity. Introducing the similarity ansatzes (2.20) into the closure relationship $u_s(x, t) = \mathcal{H}[\Gamma(x, t)]$ leads to an analogous relation $U(\eta) = \mathcal{H}[C(\eta)]$ for the similarity solutions. Since the Hilbert transform reverses parity (King 2009a), we can conclude that the only admissible parities are either U odd and C even, or U even and C odd. However, an odd function $C(\eta)$ would imply unphysical negative values of the concentration $\Gamma(x, t)$. Accordingly, we only consider similarity solutions with $U(\eta)$ odd and $C(\eta)$ even or, equivalently, $f(-\eta) = -\overline{f(\eta)}$ with the overbar indicating complex conjugation. Note that this parity requirement does not necessarily apply to the physical solutions $\Gamma(x, t)$ and $u_s(x, t)$ which, as we show in §§ 4 and 5, can be asymmetric and only attain symmetry as they converge to a self-similar solution.

In addition, similarity solutions $f(\eta)$ must satisfy a specific far-field boundary condition (Eggers & Fontelos 2008) such that the function $\psi(x, t)$ is independent of time in the far field $|x| \rightarrow \infty$. From the similarity ansatz (2.20b) and from the fact that $\alpha = \beta - 1$, it is clear that such a far-field behaviour requires $f(\eta) = O(|t - t_*|^{1-\beta})$ as $|\eta| \rightarrow \infty$. Given the definition of η in (2.20a), the only possibility to satisfy this condition is

$$f(\eta) \sim k_{\pm\infty} |\eta|^{(\beta-1)/\beta} \quad \text{as } |\eta| \rightarrow \infty. \tag{2.26}$$

We use the notation $k_{\pm\infty}$ to denote generic far-field constants that differ between k_{∞} as $\eta \rightarrow \infty$ and $k_{-\infty}$ as $\eta \rightarrow -\infty$ since, by symmetry, $k_{-\infty} = -\overline{k_{\infty}}$. Equation (2.26) is referred to as a ‘quasi-stationary’ far-field condition. If the similarity solution $f(\eta)$ is globally valid in space, then the condition is equivalent to a far-field behaviour of ψ that is constant in time as $|x| \rightarrow \infty$. If, on the other hand, $f(\eta)$ is only valid locally (as is often the case with similarity of the second kind), the condition implies that $f(\eta)$ must match with the ‘outer’ non-self-similar part of ψ , which evolves on a slower time scale.

2.3. A note on alternative formulations

The problem given by (2.16) and (2.18), as well as its variants with $Pe_s^{-1} = 0$, appear in the literature with slightly different formulations that are nonetheless equivalent, which we summarize in table 1. It is easy to check that, once transformed to our formulation, the finite-time blowup described in the mathematical literature (Baker *et al.* 1996; Morlet 1998; Chae *et al.* 2005; de la Hoz & Fontelos 2008; Eggers & Fontelos 2020) occurs for negative concentration $\Gamma < 0$. This is unphysical if Γ represents a surfactant concentration, but it is not problematic in the above body of work, where the non-local problem (2.16) has an unrelated physical motivation. Those studies describe singularities that are persistent in time and occur at points with $\Gamma < 0$, thus qualitatively different from those found here (§ 5), which happen at points of $\Gamma = 0$ within a non-negative profile $\Gamma(x) \geq 0$, and disappear at finite time. For that reason, the self-similar analysis by de la Hoz & Fontelos (2008) and Eggers & Fontelos (2020) is linearized around the non-zero value of Γ at which singularities occur, yielding different similarity equations and exponents.

3. Analysis of the advection-dominated case

In the advection-dominated case with $Pe_s^{-1} = 0$, the complexity of the similarity ODE (2.25) can be reduced by noting that it is scale invariant, since the transformations $f \rightarrow \lambda f$ and $\eta \rightarrow \lambda \eta$ (with λ real and non-zero) leave the equation unchanged. The ratio

Non-local form	Local form	Conversion to (2.16) and (2.18)	Examples
$\Gamma_t + (\mathcal{H}[\Gamma]\Gamma)_x = Pe_s^{-1}\Gamma_{xx}$ $\Gamma(x, 0) = \Gamma_0(x)$	$\psi_t + \psi\psi_x = Pe_s^{-1}\psi_{xx}$ $\psi(x, 0) = \mathcal{H}[\Gamma_0] + i\Gamma_0$	None	This work, Chae <i>et al.</i> (2005), Crowdy (2021b)
$\Gamma_t + (\tilde{\mathcal{H}}[\Gamma]\Gamma)_x = Pe_s^{-1}\Gamma_{xx}$ $\Gamma(x, 0) = \Gamma_0(x)$	$\psi_t + \psi\psi_x = Pe_s^{-1}\psi_{xx}$ $\psi(x, 0) = \tilde{\mathcal{H}}[\Gamma_0] - i\Gamma_0$	$\tilde{\mathcal{H}} \rightarrow -\mathcal{H}$ $\Gamma \rightarrow -\Gamma$ $\Gamma_0 \rightarrow -\Gamma_0$	Baker <i>et al.</i> (1996)
$\Gamma_t - \frac{1}{2}(\tilde{\mathcal{H}}[\Gamma]\Gamma)_x = 0$ $\Gamma(x, 0) = \Gamma_0(x)$	N/A	$\tilde{\mathcal{H}} \rightarrow -\mathcal{H}$ $t \rightarrow 2t$	Thess (1996)
$\Gamma_t - (\tilde{\mathcal{H}}[\Gamma]\Gamma)_x = Pe_s^{-1}\Gamma_{xx}$ $\Gamma(x, 0) = \Gamma_0(x)$	N/A	$\tilde{\mathcal{H}} \rightarrow -\mathcal{H}$	Morlet (1998)
$\Gamma_t - (\mathcal{H}[\Gamma]\Gamma)_x = 0$ $\Gamma(x, 0) = \Gamma_0(x)$	$\psi_t - \psi\psi_x = 0$ $\psi(x, 0) = \mathcal{H}[\Gamma_0] + i\Gamma_0$	$\Gamma \rightarrow -\Gamma$ $\Gamma_0 \rightarrow -\Gamma_0$ $\psi \rightarrow -\psi$	de la Hoz & Fontelos (2008), Eggers & Fontelos (2020)
$\Gamma_t + (\mathcal{H}[\Gamma]\Gamma)_x = Pe_s^{-1}\Gamma_{xx}$ $\Gamma(x, 0) = \Gamma_0(x)$	$\psi_t + \psi\psi_x = Pe_s^{-1}\psi_{xx}$ $\psi(x, 0) = \mathcal{H}[\Gamma_0] - i\Gamma_0$	$\psi \rightarrow \bar{\psi}$	Bickel & Detcheverry (2022)

Table 1. Alternative formulations of the problem found in the literature, alongside the transformations required to convert them to (2.16), (2.18) and their variants with $Pe_s^{-1} = 0$. Here, we have that $\tilde{\mathcal{H}}[\Gamma] = \pi^{-1} \int_{-\infty}^{\infty} (x' - x)^{-1} \Gamma(x', t) dx'$ is an alternative definition of the Hilbert transform, such that $\tilde{\mathcal{H}}[\Gamma] = -\mathcal{H}[\Gamma]$. Subindices indicate partial derivatives.

$f/\eta \rightarrow \lambda f/(\lambda\eta) = f/\eta$ also remains invariant under these rescalings, suggesting a change of dependent variable $g(\eta) := f(\eta)/\eta$ that turns (2.25) into

$$\frac{dg}{d \ln |\eta|} = \frac{g(1 - g)}{(g - \beta)}. \tag{3.1}$$

Equation (3.1) is a separable first-order ODE, so it can be integrated directly to obtain

$$\left(1 - \frac{f}{\eta}\right) \left(\frac{f}{\eta}\right)^{-(\beta/(\beta-1))} = k_{\pm} |\eta|^{1/(\beta-1)}, \tag{3.2}$$

where exponentiation of complex numbers is understood in a principal value sense. We again write k_{\pm} to highlight that, for complex solutions, the complex integration constant can, in principle, take different values k_+ for $\eta > 0$, and k_- for $\eta < 0$. In fact, introducing the transformations $\eta \rightarrow -\eta$ and $f \rightarrow -\bar{f}$ in (3.2), we find that

$$k_- = \bar{k}_+, \tag{3.3}$$

for solutions to have the required symmetry $f(-\eta) = -\overline{f(\eta)}$.

Equation (3.2) is still an implicit relation, providing little insight into solutions for arbitrary real values of β . It is therefore not straightforward, at least from (3.2) alone, to determine the particular subset of physically realistic similarity solutions.

3.1. The phase plane

Since (3.1) is also autonomous, its solutions can be represented in a phase plane with state variables $\text{Re}[g] = U/\eta$ and $\text{Im}[g] = C/\eta$, following Gratton & Minotti (1990). This formalism allows systematic identification of all possible similarity solutions of (2.25) as distinct trajectories in the phase plane, with the beginning of each trajectory representing the origin $\eta = 0$ and its end point indicating the far field $|\eta| \rightarrow \infty$. We construct the phase plane by first finding the fixed points of (3.1), seeding initial conditions closely around each of them, and then numerically integrating forward or backward in $\ln|\eta|$ depending on if the particular seed is along a stable or unstable direction. A detailed account of the integration procedure and the calculation of the fixed points is provided in Appendix A. We only consider exponents $\beta > 0$, excluding also $\beta = 1$ since it leads to a linear problem in (3.1) with constant solutions for $f(\eta)$.

Phase portraits of the system are shown in figure 2, for a set of six representative values of β . The phase plane has a remarkably simple structure, being symmetric with respect to the horizontal axis $C/\eta = 0$ due to the invariance of (3.1) to $g \rightarrow \bar{g}$. Note that the symmetry $f(-\eta) = -\bar{f}(\eta)$ required of the similarity solution leads to $g(-\eta) = \bar{g}(\eta)$, given that $f(\eta) = \eta g(\eta)$. In the phase plane, this means that a full solution is represented by a combination of a trajectory in the upper half-plane (given by g) and its reflection in the lower half-plane (given by \bar{g}). The curve in the upper half-plane (where $C(\eta)/\eta > 0$) represents the solution for $\eta > 0$ (since $C(\eta)$ must be non-negative), while its mirror image in the lower half-plane (where $C(\eta)/\eta < 0$) represents it for $\eta < 0$.

The fixed points of the phase plane always include two star nodes $O = (0, 0)$ and $P = (1, 0)$ on the horizontal axis, whose position is independent of the value of the exponent β . In addition, there is always a saddle point $S = (\beta, 0)$ that lies between O and P for $0 < \beta < 1$ and to the right of P for $\beta > 1$, denoting a ‘front’ where the solution is locally non-smooth. These three points O , P , and S have horizontal and vertical eigendirections. The behaviour of trajectories at the outer edges of the phase plane (i.e. as $U/\eta \rightarrow \pm\infty$ or as $C/\eta \rightarrow \pm\infty$) is given by three additional fixed points (labelled M , N and R) that the ODE (3.1) displays when it is recast in terms of the reciprocals η/U and η/C , as detailed in Appendix A. All six fixed points are listed and classified in table 2. Furthermore, the asymptotic form of the solution around each of these points can be found via linearization and is also provided in table 2, thereby listing all possible behaviours of $f(\eta)$ as $\eta \rightarrow 0$ and as $|\eta| \rightarrow \infty$ for different values of β . The fact that two trajectories (one representing $\eta > 0$ and another one $\eta < 0$) must be ‘patched’ at $\eta = 0$ to generate a full solution $f(\eta)$ results in expansions around the origin that often involve terms like $\text{sgn}(\eta)$ and $|\eta|$ (see table 2), which can only result in regular solutions for some specific values of β , as we show in § 3.2.

While all possible similarity solutions with the correct parity can be placed in the plane, not all of them are necessarily relevant from a physical standpoint. The advantage of a phase plane formalism is that it provides a way to systematically classify all trajectories in terms of the fixed points that they connect, so that they can be identified as relevant or irrelevant. We list all possible trajectories in table 3, where the rightmost column indicates whether the trajectory is classified as physically relevant, based on three criteria:

- (i) Solutions must be representative of Marangoni flow. Some trajectories in figure 2 like $M \rightarrow O$, $M \rightarrow P$ or $P \rightarrow O$ are fully contained along the horizontal axis, but that implies a zero concentration $C(\eta) = 0$ for all values of η , indicating that they do not represent Marangoni flow. In fact, the trajectory $P \rightarrow O$ along the horizontal axis for $\beta = 3/2$ (figure 2d) corresponds to the real similarity solution of the inviscid

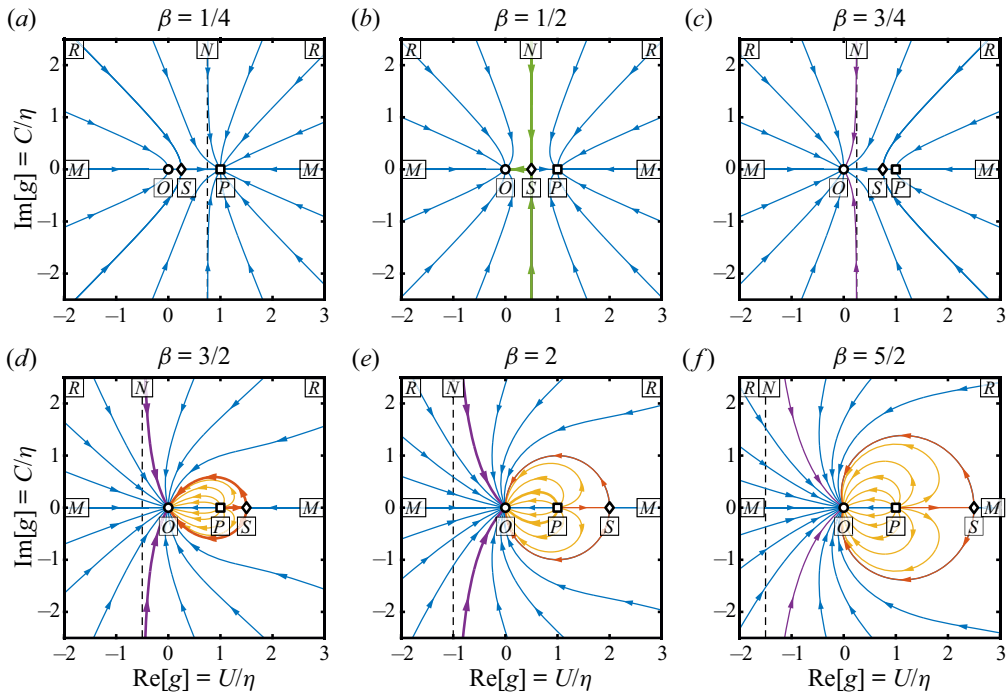


Figure 2. Phase portraits of (3.1), for six different values of $\beta > 0$, $\beta \neq 1$. Any given two trajectories that are symmetric with respect to the horizontal axis represent one possible similarity solution $f(\eta) = \eta g(\eta)$, with the origin of the trajectory denoting $\eta = 0$ and the endpoint denoting $|\eta| \rightarrow \infty$. The three fixed points $O = (0, 0)$ (stable node), $P = (1, 0)$ (node) and $S = (\beta, 0)$ (saddle) have horizontal and vertical eigendirections for all $\beta > 0$. Points M, N, R are the fixed points of the ODE satisfied by the reciprocals of the solution (see Appendix A). Only green, purple, orange and yellow trajectories represent similarity solutions that are physically relevant, as illustrated in table 3. Stability criteria (§ 3.2) select the only five solutions that can be obtained in practice, which are highlighted with a wider streak. The dashed vertical line corresponds to $U/\eta = 1 - \beta$.

Burgers equation (2.19a) described by Eggers & Fontelos (2008), which appears prior to the formation of a shock and is relevant to describe other problems like gas dynamics or wave breaking.

- (ii) Solutions must have a far-field behaviour compatible with (2.26), as explained in § 2.2. Accordingly, all trajectories listed in table 2 with a far field incompatible with (2.26), such as those ending at point P for $0 < \beta < 1$, are labelled as irrelevant.
- (iii) Solutions must be continuous at the origin. For instance, solutions starting at points M or R have an odd but discontinuous velocity $U(\eta)$ at $\eta = 0$, with $U(0^+) = K$ and $U(0^-) = -K$ for some real, non-zero constant K , as detailed in table 2.

Based on this classification outlined in table 3, we identify four families of solutions that qualify as physically relevant. We can interpret the qualitative behaviour of each of these trajectories depending on their position within the phase plane, following the discussion given in Appendix B. Trajectory $N \rightarrow S \rightarrow O$, which only exists for $\beta = 1/2$, is highlighted in green in figure 2 and, according to Appendix B, corresponds to a ‘spreading’ similarity solution with a forward-time definition of the similarity variable, as in (2.22a). We discuss this spreading solution, as well as its counterpart with finite diffusion, in § 4. The $P \rightarrow O$ (yellow in figure 2) and $P \rightarrow S \rightarrow O$ (orange in figure 2) trajectories are ‘filling’ similarity solutions with a backward-time scaling as in (2.22b),

Fixed point $\left(\frac{U}{\eta}, \frac{C}{\eta}\right)$	Type	Meaning	$U(\eta) \sim$	$C(\eta) \sim$
$O(0, 0)$	SN	$ \eta \rightarrow \infty$	$K \operatorname{sgn}(\eta) \eta ^{(\beta-1)/\beta}$ $K^2 \frac{(\beta-1)}{\beta} \operatorname{sgn}(\eta) \eta ^{(\beta-2)/\beta}$ $K \operatorname{sgn}(\eta) \eta ^{(\beta-1)/\beta}$	0 $K \eta ^{(\beta-1)/\beta}$ $K' \eta ^{(\beta-1)/\beta}$
$P(1, 0)$	SN [$0 < \beta < 1$]	$ \eta \rightarrow \infty$	$\eta + K \operatorname{sgn}(\eta) \eta ^{\beta/(\beta-1)}$	0
	UN [$\beta > 1$]	$\eta = 0$	$\eta + \frac{K^2 \beta}{(1-\beta)} \operatorname{sgn}(\eta) \eta ^{(\beta+1)/(\beta-1)}$ $\eta + K \operatorname{sgn}(\eta) \eta ^{\beta/(\beta-1)}$	$K \eta ^{\beta/(\beta-1)}$ $K' \eta ^{\beta/(\beta-1)}$
$S(\beta, 0)$	S	Front at $\eta = \eta_f$	$\beta \eta \pm \eta \ln^{1/2} \left(\left \frac{\eta}{\eta_f} \right ^{2\beta(1-\beta)} \right)$	0
			$\beta \eta$	$ \eta \ln^{1/2} \left(\left \frac{\eta_f}{\eta} \right ^{2\beta(1-\beta)} \right)$
$M(\pm\infty, 0)$	S	$\eta = 0$	$K \operatorname{sgn}(\eta)$	0
$N(1-\beta, \pm\infty)$	S	$\eta = 0$	$(1-\beta)\eta + \frac{\beta(1-\beta)(1-2\beta)}{3K^2} \eta^3$	$K - \frac{\beta(1-\beta)}{2K} \eta^2$
$R(\pm\infty, \pm\infty)$	UN	$\eta = 0$	$K \operatorname{sgn}(\eta)$	K'

Table 2. Fixed points of the ODE system given by the real and imaginary parts of (3.1), for $\beta > 0$ and $\beta \neq 1$; SN denotes a stable node, UN an unstable node, and S a saddle. Points M , N and R are obtained as fixed points of ODE systems involving the reciprocals η/U and η/C , as detailed in Appendix A. The entries for $U(\eta)$ and $C(\eta)$ denote every possible asymptotic expansion about each fixed point, where K and K' are independent, real, non-zero constants of integration, and η_f is the (real, non-zero) location of the front occurring at the saddle point S . When more than one entry for $U(\eta)$ and $C(\eta)$ is provided, the first row corresponds to the trajectory along the horizontal eigendirection, the second row to the trajectory along the vertical eigendirection and the third (if provided) to generic curves along any other direction.

which suggests they are valid immediately prior to a singularity. They only hold locally as evidenced by their far-field behaviour, since these solutions only exist for $\beta > 1$ and the condition (2.26), $f(\eta) \sim k_{\pm\infty} |\eta|^{(\beta-1)/\beta}$, then implies that they grow unbounded as $|\eta| \rightarrow \infty$. The Hilbert transform is undefined for unbounded functions so, as observed by Thess *et al.* (1997), similarity solutions for $\beta > 1$ must be only valid locally. The last of these four families of solutions is $N \rightarrow O$, which exists for $\beta > 1/2$, is displayed in purple in figure 2 and has forward-time scaling as in (2.22a). These solutions can be either spreading, for $1/2 < \beta < 1$, or filling, for $\beta > 1$.

Three of the identified families of curves, namely $P \rightarrow O$ (yellow), $P \rightarrow S \rightarrow O$ (orange) and $N \rightarrow O$ (purple), appear to exist for multiple values of β , which is typical of self-similarity of the second kind (Barenblatt 1996). In the case of $P \rightarrow O$, there are even several possible solutions within the same value of β . These second-kind solutions appear around finite-time singularities, and we show in § 3.2 how considerations about their stability rule out many of the trajectories within these three families, leading to the only solutions that are truly obtainable in practice.

Trajectory	Range of β	Physically relevant trajectory?
$M \rightarrow O$	$\beta > 0$	No, $U(0^-) \neq U(0^+)$ and $C(\eta) = 0$.
$R \rightarrow O$	$\beta > 0$	No, $U(0^-) \neq U(0^+)$.
$N \rightarrow P$	$0 < \beta < 1/2$	No, invalid far field.
$M \rightarrow P$	$0 < \beta < 1$	No, $U(0^-) \neq U(0^+)$, $C(\eta) = 0$, and invalid far field.
$R \rightarrow P$	$0 < \beta < 1$	No, $U(0^-) \neq U(0^+)$ and invalid far field.
$R \rightarrow S \rightarrow O$	$0 < \beta < 1, \beta \neq 1/2$	No, $U(0^-) \neq U(0^+)$.
$R \rightarrow S \rightarrow P$	$0 < \beta < 1, \beta \neq 1/2$	No, $U(0^-) \neq U(0^+)$ and invalid far field.
$N \rightarrow S \rightarrow O$	$\beta = 1/2$	Yes, green trajectory in figure 2.
$N \rightarrow S \rightarrow P$	$\beta = 1/2$	No, invalid far field.
$N \rightarrow O$	$\beta > 1/2$	Yes, purple trajectories in figure 2.
$M \rightarrow S \rightarrow O$	$\beta > 1$	No, $U(0^-) \neq U(0^+)$.
$P \rightarrow S \rightarrow O$	$\beta > 1$	Yes, orange trajectories in figure 2.
$P \rightarrow O$	$\beta > 1$	Depends on its direction around point P : <ul style="list-style-type: none"> • Horizontal: no, $C(\eta) = 0$. • Otherwise: yes, yellow trajectories in figure 2.

Table 3. List of all possible phase-plane trajectories of the reduced similarity ODE (3.1), for different values of the exponent β . The last column indicates whether a given trajectory represents a physically relevant solution. If the solution is classified as not relevant, the reasons are provided, based on three criteria: (i) having a non-zero concentration $C(\eta) \neq 0$ representative of Marangoni flow, (ii) compatibility with the far-field condition (2.26) and (iii) continuity at $\eta = 0$. If the trajectory is physically relevant, its colour in figure 2 is indicated.

3.2. Stability analysis

In order to analyse the stability of similarity solutions, we use the dynamical system formulation (see Giga & Kohn 1985, 1987; Eggers & Fontelos 2008, 2015) of the inviscid Burgers equation (2.19a). Instead of seeking to reduce the two physical variables x and t into a single similarity variable η , we use the more general change of variables

$$\psi(x, t) = A|t - t_*|^{\beta-1}F(\eta, \tau), \tag{3.4a}$$

$$\eta = \text{sgn}(t - t_*) \frac{x - x_*}{A|t - t_*|^\beta}, \tag{3.4b}$$

$$\tau = -\ln|t - t_*|, \tag{3.4c}$$

which, instead of reducing the original partial differential equation (PDE) to an ODE, leads to a partial differential equation for $F(\eta, \tau)$

$$\frac{\partial F}{\partial \tau} = \left[(F - \beta\eta) \frac{\partial F}{\partial \eta} - (1 - \beta)F \right]. \tag{3.5}$$

The key of the transformation given by (3.4) is that the steady state of (3.5) reduces to the similarity equation (2.25). Indeed, the definition (3.4c) of τ indicates that approaching the singularity time $t \rightarrow t_*$ corresponds to $\tau \rightarrow \infty$, leading to a steady state $\partial_\tau F \rightarrow 0$ at which solutions to (3.5) satisfy the similarity ODE (2.25).

The stability of each of the similarity solutions found in § 3.1 can now be determined via linear stability analysis around $f(\eta)$. We pose a perturbation

$$F(\eta, \tau) = f(\eta) + \varepsilon \sum_{n=0}^{\infty} b_n e^{\nu_n \tau} \phi_n(\eta) + O(\varepsilon^2), \tag{3.6}$$

where $\varepsilon \ll 1$, ν_n are the growth rates of each mode ϕ_n and b_n are the mode amplitudes. Introducing (3.6) into the PDE (3.5) we obtain at order $O(\varepsilon)$ an eigenvalue problem

$$\mathcal{L}\phi_n := \left[\frac{\beta(1-\beta)}{(f-\beta\eta)}\eta + (f-\beta\eta)\frac{d}{d\eta} \right] \phi_n = \nu_n\phi_n. \tag{3.7}$$

The stability of any given similarity solution $f(\eta)$ can then be determined solving the eigenvalue problem (3.7) for the linear operator \mathcal{L} , which itself depends on the similarity solution $f(\eta)$. Moreover, the spectrum of \mathcal{L} is typically discrete given some additional conditions for the eigenfunctions ϕ_n (Eggers & Fontelos 2008, 2015). Namely, each $\phi_n(\eta)$ must be regular at $\eta = 0$, and satisfy its own quasi-stationary far-field condition

$$\phi_n(\eta) \sim k_{\pm\infty}|\eta|^{(\beta-1-\nu_n)/\beta} \quad \text{as } |\eta| \rightarrow \infty, \tag{3.8}$$

for some complex constants $k_{\pm\infty}$. Only those similarity solutions leading to a spectrum of \mathcal{L} with negative eigenvalues $\nu_n < 0$ result in perturbations decaying in time and are therefore stable. However, as shown by Eggers & Fontelos (2008, 2015), there is also a specific subset of non-negative eigenvalues that does not lead to instability and is instead an artefact of the continuous symmetries of the problem. Specifically, the invariance of the governing equation (2.19a) to shifts in space $x \rightarrow x + \lambda$, shifts in time $t \rightarrow t + \lambda$ and scalings $\psi \rightarrow \lambda\psi$, $t \rightarrow \lambda t$, $x \rightarrow \lambda^2 x$, always leads to the three eigenvalues $\nu = \beta$, $\nu = 1$ and $\nu = 0$, respectively (see § 3.2 in Eggers & Fontelos 2015). Accordingly, we look for solutions from the phase plane that lead to a spectrum of \mathcal{L} with at most these three non-negative eigenvalues, with all others being negative.

The three families of trajectories in figure 2 considered here ($P \rightarrow O$, $P \rightarrow S \rightarrow O$ and $N \rightarrow O$) all have the same far-field behaviour since they end at the same point. From table 2, we know that $f(\eta) \sim k_{\pm\infty}|\eta|^{(\beta-1)/\beta}$ as $|\eta| \rightarrow \infty$, which can be introduced in the eigenvalue problem (3.7) to yield the far-field behaviour of the eigenfunctions

$$\frac{d\phi_n}{d\eta} = \left[\frac{\nu_n(f-\beta\eta) - \beta(1-\beta)\eta}{(f-\beta\eta)^2} \right] \phi_n \sim \left[\frac{\beta-1-\nu_n}{\beta\eta} \right] \phi_n \quad \text{as } |\eta| \rightarrow \infty, \tag{3.9}$$

which leads to $\phi_n \sim k_{\pm\infty}|\eta|^{(\beta-1-\nu_n)/\beta}$ in the far field, in agreement with condition (3.8). This means that, for these three families of trajectories, the required far-field behaviour of eigenfunctions $\phi_n(\eta)$ is satisfied automatically, and the eigenvalues are then solely determined by the regularity of $\phi_n(\eta)$ at $\eta = 0$, as shown in the next three subsections.

3.2.1. Trajectories $P \rightarrow O$ (yellow in figure 2)

Table 2 indicates that all $P \rightarrow O$ solutions that do not depart P along the vertical eigendirection have expansions $U(\eta) \sim \eta + K \operatorname{sgn}(\eta) |\eta|^\omega$ and $C(\eta) \sim K' |\eta|^\omega$, where we define the exponent $\omega := \beta/(\beta-1)$. The only possibility for $U(\eta)$ to be regular at the origin is for ω to be an odd integer (so that $\operatorname{sgn}(\eta) |\eta|^\omega = \eta^\omega$), whereas the only possibility for $C(\eta)$ to be regular is for ω to be an even integer (so that $|\eta|^\omega = \eta^\omega$). Since these requirements cannot be fulfilled simultaneously, these generic trajectories $P \rightarrow O$ can never be regular at $\eta = 0$. However, the specific $P \rightarrow O$ trajectory that departs P along the vertical eigendirection has a different expansion, given by table 2 as $f(\eta) \sim \eta + iK|\eta|^\omega + [K^2\beta/(\beta-1)] \operatorname{sgn}(\eta) |\eta|^{2\omega-1}$. In that case, the expression can be regular if ω is an even integer, turning into a true polynomial expansion. In other words,

from the continuum of possible real values $\beta > 1$, only a discrete set β_m given by

$$\frac{\beta_m}{\beta_m - 1} = 2m + 2, \quad \text{with } m = 0, 1, 2, \dots, \tag{3.10}$$

leads to regular solutions at the origin, and only for the trajectory leaving P along the vertical direction. The possible similarity exponents are then

$$\beta_m = \frac{2m + 2}{2m + 1} = 2, \frac{4}{3}, \frac{6}{5}, \frac{8}{7}, \dots \tag{3.11}$$

Each value β_m in this discrete set results in a solution $f_m(\eta)$ with an expansion $f_m(\eta) \sim \eta + iK\eta^{2m+2} + K^2(2m + 2)\eta^{4m+3}$ around the origin. Moreover, each of these solutions leads to a discrete set of eigenfunctions ϕ_{mn} and eigenvalues v_{mn} indexed by an integer n . Inserting the expansion for $f_m(\eta)$ in the eigenvalue problem (3.7), we obtain

$$\frac{d\phi_{mn}}{d\eta} \sim \frac{(2m + 2) - v_{mn}(2m + 1)}{\eta} \phi_{mn} \quad \text{as } \eta \rightarrow 0, \tag{3.12}$$

which implies that eigenfunctions are of the form

$$\phi_{mn}(\eta) \sim k \eta^{[(2m+2)-v_{mn}(2m+1)]} \quad \text{as } \eta \rightarrow 0, \tag{3.13}$$

and therefore for ϕ_{mn} to be smooth at the origin we require an integer exponent

$$(2m + 2) - v_{mn}(2m + 1) = n, \quad \text{with } n = 0, 1, 2, \dots \tag{3.14}$$

This leads to the discrete set of eigenvalues

$$v_{mn} = \frac{2m - n + 2}{2m + 1}, \quad \text{with } m = 0, 1, 2, \dots \text{ and } n = 0, 1, 2, \dots \tag{3.15}$$

As detailed in Eggers & Fontelos (2008), a spectrum of eigenvalues with this ‘ladder structure’ is quite general in the self-similar description of singularities. The smallest exponent $\omega = \beta/(\beta - 1)$, which is given by $m = 0$, defines a ‘ground state’ solution

$$m = 0 \implies \beta = \beta_0 = 2, \quad v_{0n} = 2, 1, 0, -1, -2, \dots \tag{3.16}$$

The three non-negative eigenvalues $v_{00} = \beta = 2$, $v_{01} = 1$ and $v_{02} = 0$ are an artefact of the problem symmetries and, as explained by Eggers & Fontelos (2015), do not result in instability since their associated modes in (3.6) can be cancelled by a shift in the constants t_* , x_* and A that enter the similarity variables (3.4). All other eigenvalues are negative, so we conclude that this ground state solution $f_0(\eta)$ is stable.

Higher values of m define ‘excited states’, such as the first two

$$m = 1 \implies \beta = \beta_1 = \frac{4}{3}, \quad v_{1n} = \frac{4}{3}, 1, \frac{2}{3}, \frac{1}{3}, 0, -\frac{1}{3}, -\frac{2}{3}, \dots, \tag{3.17a}$$

$$m = 2 \implies \beta = \beta_2 = \frac{6}{5}, \quad v_{2n} = \frac{6}{5}, 1, \frac{4}{5}, \frac{3}{5}, \frac{2}{5}, \frac{1}{5}, 0, -\frac{1}{5}, -\frac{2}{5}, \dots \tag{3.17b}$$

These excited states include the three eigenvalues $v = \beta$, $v = 1$, $v = 0$ that do not correspond to instability, but they also have an increasing number of other positive eigenvalues that make them unstable. Since unstable similarity solutions cannot occur in reality, these excited states are unphysical.

In summary, the only trajectory $P \rightarrow O$ leading to a physical solution is the one leaving P along the vertical for $\beta = 2$, which corresponds to the yellow trajectory highlighted

with a wider streak in figure 2(e). We show in § 5.1 that the similarity solution $f(\eta)$ can in this case be obtained in closed form, and that it appears when a locally depleted distribution of surfactant tends to become uniform under the action of Marangoni flow. Such a distribution, which we call a ‘dimple’ (following Bickel & Detcheverry 2022), must have zero concentration $\Gamma_0(x_0) = 0$ with a quadratic minimum $\Gamma_0 \sim K(x - x_0)^2$ for some $x = x_0$. Self-similarity appears prior to the time t_* at which the dimple ‘closes’, and thus we call this the ‘dimple closure’ solution.

3.2.2. Trajectories $P \rightarrow S \rightarrow O$ (orange in figure 2)

We can proceed analogously to determine the only exponent β that leads to stability for the $P \rightarrow S \rightarrow O$ solution. From table 2, the expansion around P for trajectories departing along the horizontal eigendirection is $f(\eta) \sim \eta + K \operatorname{sgn}(\eta) |\eta|^\omega$, with $\omega := \beta/(\beta - 1)$. This solution can only be regular at the origin if the exponent ω is odd, excluding $\omega = 1$ since it cannot be achieved for any finite β . We then have the discrete sequence

$$\frac{\beta_m}{\beta_m - 1} = 2m + 3, \quad \text{with } m = 0, 1, 2, \dots, \tag{3.18}$$

which results in exponents given by

$$\beta_m = \frac{2m + 3}{2m + 2} = \frac{3}{2}, \frac{5}{4}, \frac{7}{6}, \frac{9}{8}, \dots \tag{3.19}$$

This set of values leads to local expansions $f_m(\eta) \sim \eta + K\eta^{2m+3}$ around $\eta = 0$. Introducing this expansion for $f_m(\eta)$ in the eigenvalue problem (3.7), we obtain

$$\frac{d\phi_{mn}}{d\eta} \sim \frac{(2m + 3) - v_{mn}(2m + 2)}{\eta} \phi_{mn} \quad \text{as } \eta \rightarrow 0, \tag{3.20}$$

which leads to eigenfunctions $\phi_{mn} \sim k \eta^{[(2m+3)-v_{mn}(2m+2)]}$ locally around $\eta = 0$. The functions ϕ_{mn} are then smooth only if

$$(2m + 3) - v_{mn}(2m + 2) = n, \quad \text{with } n = 0, 1, 2, \dots \tag{3.21}$$

This means that the discrete sequence of eigenvalues for the $P \rightarrow S \rightarrow O$ trajectory is

$$v_{mn} = \frac{2m - n + 3}{2m + 2}, \quad \text{with } m = 0, 1, 2, \dots \text{ and } n = 0, 1, 2, \dots \tag{3.22}$$

This spectrum of eigenvalues is identical to that of the real inviscid Burgers equation, for which Eggers & Fontelos (2008) show there exists a similarity solution of the second kind with $\beta = 3/2$ immediately prior to the formation of a shock. This should not come as a surprise, since that (real) similarity solution is simply the $P \rightarrow O$ trajectory along the horizontal axis in figure 2(e). This $P \rightarrow O$ solution and the $P \rightarrow S \rightarrow O$ solution both depart P along the horizontal eigendirection, so they have the same leading-order structure around $\eta = 0$ and thus the same spectrum. Similar to the previous case of § 3.2.1, the

eigenvalues (3.22) lead to states of the form

$$m = 0 \implies \beta = \beta_0 = \frac{3}{2}, \quad \nu_{0n} = \frac{3}{2}, 1, \frac{1}{2}, 0, -\frac{1}{2}, -1, \dots, \quad (3.23a)$$

$$m = 1 \implies \beta = \beta_1 = \frac{5}{4}, \quad \nu_{1n} = \frac{5}{4}, 1, \frac{3}{4}, \frac{1}{2}, \frac{1}{4}, 0, -\frac{1}{4}, -\frac{1}{2}, \dots, \quad (3.23b)$$

$$m = 2 \implies \beta = \beta_2 = \frac{7}{6}, \quad \nu_{2n} = \frac{7}{6}, 1, \frac{5}{6}, \frac{2}{3}, \frac{1}{2}, \frac{1}{3}, \frac{1}{6}, 0, -\frac{1}{6}, -\frac{1}{3}, \dots \quad (3.23c)$$

All states contain the eigenvalues $\nu = \beta$, $\nu = 1$ and $\nu = 0$ that do not lead to instabilities, but also have other positive eigenvalues that seemingly imply that no stable similarity solutions exist. However, in the particular case of the ground-state solution $m = 0$, the additional positive eigenvalue $\nu = 1/2$ does not necessarily lead to instability either, as shown by Eggers & Fontelos (2008) in the case of the real solution. This can be shown particularizing the expansion (3.6) at the position $x = x_*$ (or $\eta = 0$) of the singularity

$$\left. \frac{\partial^2 F_0}{\partial \eta^2} \right|_{\eta=0} = f_0''(0) + \varepsilon \left[b_{02} e^{\tau/2} \phi_{02}''(0) + \sum_{\substack{n=0 \\ n \neq 2}}^{\infty} b_{0n} e^{\nu_{0n} \tau} \phi_{0n}''(0) \right] + O(\varepsilon^2). \quad (3.24)$$

Since we have deduced that for the ground state $m = 0$ we have $f_0(\eta) \sim \eta + K\eta^3$ and $\phi_{0n}(\eta) \sim k\eta^n$ around the origin, then we have that $f_0''(0) = 0$ and $\phi_{0n}''(0) = 0$ for all modes with $n \neq 2$, cancelling out the first and third terms on the right-hand side of (3.24). Also, we have that $\phi_{02}''(0) \neq 0$ in the second term above. However, in the particular case where the second derivative of the solution is zero at the position of the singularity, i.e. $\partial_{xx}\psi(x_*, t) = 0$, we also have $\partial_{\eta\eta}F(0, \tau) = 0$ and therefore the amplitude b_{02} must be zero. In that case, $b_{02} = 0$ cancels the $n = 2$ mode altogether and the positive eigenvalue $\nu = 1/2$ is irrelevant in the stability of the solution. As a consequence, the ground state $m = 0$ is stable for the particular set of initial conditions that lead to $\partial_{xx}\psi = 0$ at the position of the singularity. In the case of the real similarity solution studied by Eggers & Fontelos (2008), one can show that this is always satisfied in a suitable frame of reference for solutions that develop a shock (see Appendix D). However, the condition is not necessarily satisfied in the complex case. In fact, we show in § 5 that only if the initial distribution of surfactant is locally depleted with $\Gamma_0(x_0) = 0$ for some $x = x_0$, and is also ‘flatter’ than quadratic (i.e. if $\Gamma_0''(x_0) = 0$), then the condition $\partial_{xx}\psi(x_*, t) = 0$ is fulfilled and the self-similar solution before the singularity is then $P \rightarrow S \rightarrow O$ with $\beta = 3/2$. We call these flatter surfactant profiles ‘holes’, in order to distinguish them from dimples with a sharper quadratic minimum.

In conclusion, $\beta = 3/2$ is the only exponent leading to stability for $P \rightarrow S \rightarrow O$, corresponding to the trajectory highlighted in figure 2(d). Only filling solutions that have $\partial_{xx}\psi = 0$ at the singularity, which we call ‘holes’, can lead to this similarity solution, which we correspondingly call the ‘hole closure’ solution. We show in § 5.2 that $f(\eta)$ can in this case also be obtained in closed form.

3.2.3. Trajectories $N \rightarrow O$ (purple in figure 2)

The similarity solution $N \rightarrow O$ has a functional form $f(\eta) \sim iK + (1 - \beta)\eta$ around $\eta = 0$ (see table 2), appearing to always be smooth at the origin $\eta = 0$ independently of β .

Furthermore, inserting it into the eigenvalue problem (3.7), we obtain

$$\frac{d\phi_n}{d\eta} \sim i\nu_n\phi_n \quad \text{as } \eta \rightarrow 0, \tag{3.25}$$

which always leads to smooth eigenfunctions $\phi_n \sim ke^{i\nu_n\eta}$ around $\eta = 0$. The absence of an evident sequence of discrete solutions or eigenfunctions based on regularity suggests that the behaviour of the $N \rightarrow O$ solution could be governed by a more complicated continuum of possible similarity solutions (as in Eggers 2000).

Analysing every possible exponent for the $N \rightarrow O$ solution is beyond the scope of this paper, but we will consider the two specific cases of $\beta = 3/2$ and $\beta = 2$. Since, according to Appendix B, $N \rightarrow O$ can be interpreted as a forward-time solution happening subsequent to a singularity, it must appear immediately after either the ‘dimple closure’ solution or the ‘hole closure’ solution, since both occur immediately before the singularity. Furthermore, since the far-field scaling of solutions is intimately linked to the similarity exponents through the condition (2.26), the exponent of the pre-singularity solution fixes the exponent of the post-singularity $N \rightarrow O$ solution, otherwise the far-field behaviour of the solution would change instantly at $t = t_*$. We can then ensure that $\beta = 3/2$ and $\beta = 2$ are possible exponents for the $N \rightarrow O$ solution, as we confirm in § 5. Following the naming convention used by Zheng *et al.* (2018) for capillary films, we use the term ‘levelling’ for these two solutions in which the concentration levels towards $\Gamma \rightarrow 1$, as opposed to the pre-singularity ‘closure’ solutions where the concentration remains $\Gamma = 0$ at the point of the singularity. Specifically, we call the $N \rightarrow O$ solution with $\beta = 2$ the ‘dimple levelling’ solution (highlighted in figure 2e), since it follows the ‘dimple closure’ solution, whereas the $N \rightarrow O$ solution with $\beta = 3/2$ is labelled as the ‘hole levelling’ solution (highlighted in figure 2d) since it comes after the ‘hole closure’ solution. These solutions are obtained in closed form in §§ 5.1 and 5.2, respectively.

4. Spreading solutions

In the case of a spreading pulse, depicted in figure 1(a), the total mass of (insoluble) surfactant is, in general, conserved and imposed by the initial profile $\Gamma_0(x)$. This can be realized by direct integration of (2.3) in x , as we show in Appendix C. We define the total (dimensionless) mass M_0 as

$$M_0 := \int_{-\infty}^{\infty} \Gamma(x, t) \, dx = \int_{-\infty}^{\infty} \Gamma_0(x) \, dx, \tag{4.1}$$

which, upon substitution of the similarity ansatzes (2.20a) and (2.21b), and using $A = B$ and a forward-time description $t > t_*$ as discussed in § 2.2, leads to

$$M_0 = A^2(t - t_*)^{\alpha+\beta} \int_{-\infty}^{\infty} C(\eta) \, d\eta. \tag{4.2}$$

The above relation is only compatible with self-similar behaviour if the additional requirement $\alpha + \beta = 0$ is met, in which case the solution $f(\eta)$ must also satisfy

$$\int_{-\infty}^{\infty} C(\eta) \, d\eta = \frac{M_0}{A^2}. \tag{4.3}$$

4.1. Advection-dominated limit

For the limit of zero diffusion $Pe_s^{-1} = 0$, the requirement $\alpha = \beta - 1$ from the similarity ODE (2.23), combined with $\alpha = -\beta$ from the integral constraint (4.2), leads to $\alpha = -1/2$ and $\beta = 1/2$. Since the exponents can be fixed *a priori* only from dimensional analysis, this solution displays self-similarity of the first kind (Barenblatt 1996). This solution corresponds to the $N \rightarrow S \rightarrow O$ trajectory in figure 2(b), as shown in § 3.

For these particular values of the exponents α and β , an explicit solution can be obtained from the implicit relationship (3.2). For $\beta = 1/2$, (3.2) yields

$$f^2 - \eta f + k_{\pm} = 0. \tag{4.4}$$

The case of a pulse solution requires $f(0) = iC(0)$ to be imaginary, which applied to (4.4) leads to real integration constants k_{\pm} . Added to the required symmetry condition $k_- = \bar{k}_+$ (3.3), this means that we can consider only a single real constant $k = k_+ = k_-$. Furthermore, and since solutions to the similarity ODE (2.25) are defined only up to a rescaling of f and η , we choose $k = 1$ to fix $f(0) = i$ and, by extension, $C(0) = 1$. The quadratic equation can be solved, leading to

$$f(\eta) = \frac{1}{2} \left(\eta \pm \sqrt{\eta^2 - 4} \right), \tag{4.5}$$

where the root symbol is always taken to indicate the principal root. The choice of sign must be made at each value of η to ensure that the concentration $\text{Im}[f]$ remains positive and that the far field complies with condition (2.26). These conditions lead to a particularly compact final form of the solution

$$f(\eta) = \frac{1}{2} \left(\eta + \sqrt{2 - \eta} \sqrt{-2 - \eta} \right). \tag{4.6}$$

The complex form (4.6) can be split into its real and imaginary parts to yield the similarity solutions $U(\eta)$ and $C(\eta)$ separately, which can be defined piecewise as

$$C(\eta) = \begin{cases} \frac{1}{2} \sqrt{4 - \eta^2}, & \text{if } |\eta| \leq 2, \\ 0, & \text{if } |\eta| \geq 2. \end{cases} \tag{4.7a}$$

$$U(\eta) = \begin{cases} \frac{\eta}{2}, & \text{if } |\eta| \leq 2, \\ \frac{1}{2} \text{sgn}(\eta) \left[|\eta| - \sqrt{\eta^2 - 4} \right], & \text{if } |\eta| \geq 2. \end{cases} \tag{4.7b}$$

Note that, since $\int_{-\infty}^{\infty} C(\eta) d\eta = \pi$, in order to satisfy the integral constraint (4.3) the constant A in the similarity ansatz (2.20) must be chosen as

$$A = \sqrt{\frac{M_0}{\pi}}. \tag{4.8}$$

Figure 3 displays three distinct spreading pulses of surfactant (whose initial profiles $\Gamma_0(x)$ can be found in Appendix E) obtained solving the inviscid Burgers equation (2.19a) via the method of characteristics (Crowdy 2021b). At large times $t \gg 1$, the curves are shown to collapse onto the similarity solution (4.6), which is equivalent to the one originally identified by Thess (1996) through different methods. As pointed out by Bickel & Detcheverry (2022), a Cauchy pulse (figure 3a), which decays as $\Gamma \sim x^{-2}$ in the far

Self-similarity in unbounded viscous Marangoni flows

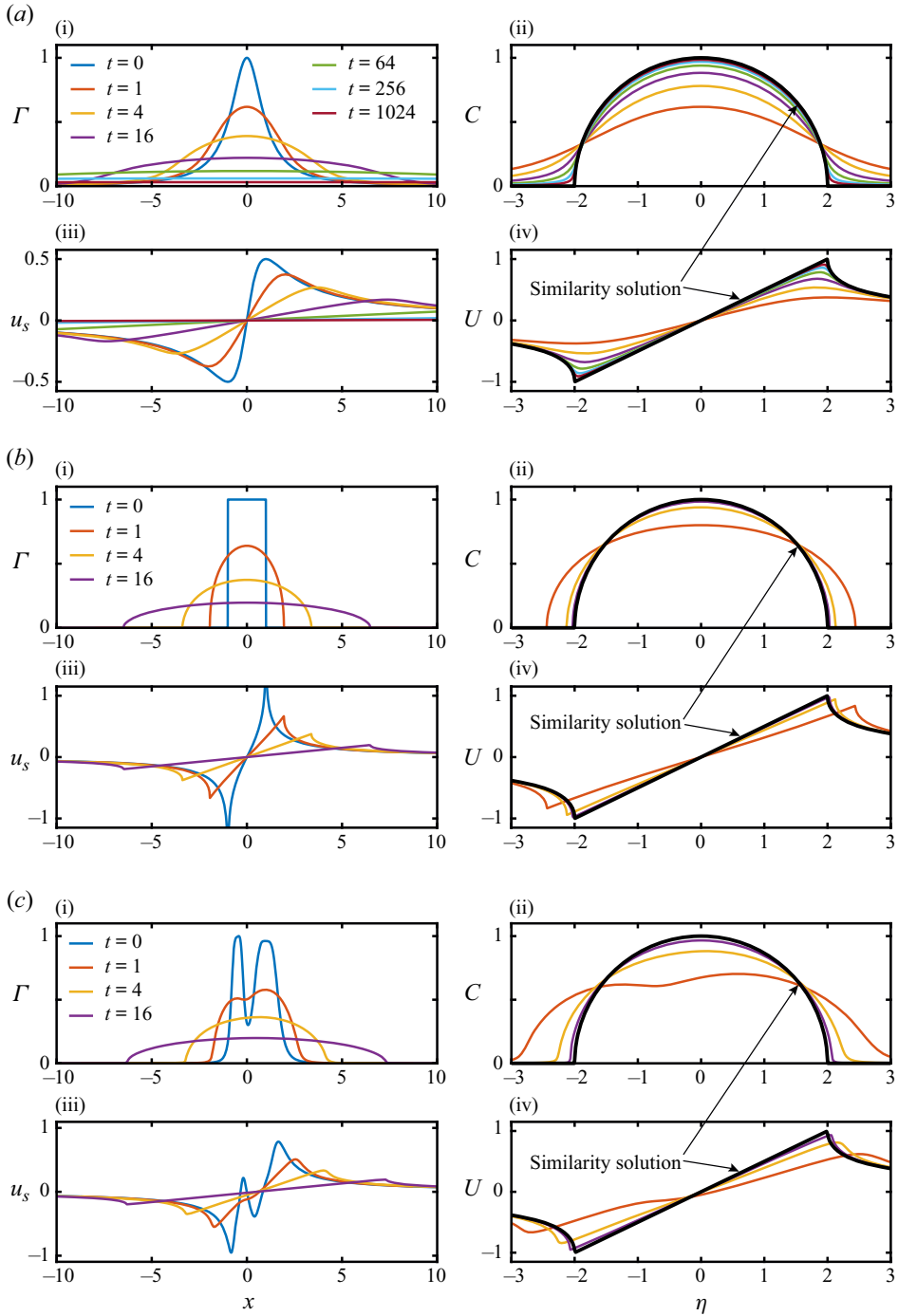


Figure 3. Spreading solutions with $Pe_s^{-1} = 0$, for initial profiles of surfactant given by (a) a Cauchy pulse, (b) a rectangular pulse and (c) a double quartic pulse, with their functional forms given in Appendix E. For each example, panels (a i,iii,b i,iii,c i,iii) show the concentration $\Gamma(x, t)$ and interfacial velocity $u_s(x, t)$ obtained through the exact solution of (2.19), while panels (a ii,iv,b ii,iv,c ii,iv) show the same data rescaled in similarity variables (colour curves), superimposed on the similarity solution (4.7) (black curves) valid at long times $t \gg 1$. For the double quartic pulse (c), the reference position in (2.20) is $x_* = 1/2$; in all other examples $x_* = t_* = 0$.

field, requires very large times of order $t = O(10^3)$ to become visually indistinguishable from the similarity solution. However, figure 3(b,c) illustrate how pulses with a faster decay or compact support require much shorter times, $t = O(10)$ to converge to (4.6).

It is worth noting that the initial profile $\Gamma_0(x)$ of the double quartic pulse of figure 3(c) is asymmetric, and therefore the centre x_* of the distribution at long times is non-zero. We show in Appendix C that the first moment of the surfactant distribution

$$M_1 := \int_{-\infty}^{\infty} x\Gamma(x, t) dx = \int_{-\infty}^{\infty} x\Gamma_0(x) dx, \tag{4.9}$$

is a conserved invariant of the problem, provided the above integral exists. This leads to a straightforward definition of the reference position x_* for pulses, namely

$$x_* = \frac{\int_{-\infty}^{\infty} x\Gamma_0(x) dx}{\int_{-\infty}^{\infty} \Gamma_0(x) dx} = \frac{M_1}{M_0}. \tag{4.10}$$

In the case of figure 3(c), we have that $x_* = 1/2$ (see Appendix E), as can be evidenced by the shifted pulse at long times in panel (c i).

4.2. General case with finite diffusion

For general values of $Pe_s^{-1} > 0$, (2.23) requires both exponents to be fixed $\alpha = -1/2$ and $\beta = 1/2$. These values happen to also be compatible with the additional requirement $\alpha + \beta = 0$ from the integral constraint (4.2), illustrating that this more general case with diffusion also displays self-similar solutions of the first kind. The governing ODE given by (2.24) can be integrated directly, leading to

$$\frac{df}{d\eta} = k_1 - \eta f + f^2, \tag{4.11}$$

where the constant k_1 must be real since, for pulses, $f(0) = iC(0)$ is imaginary and $f'(0) = U'(0)$ is real by symmetry. The far-field condition (2.26), which in this case with $\beta = 1/2$ translates to $f \sim k_\infty \eta^{-1}$ as $\eta \rightarrow \infty$, can be introduced in (4.11) to obtain that $k_1 = k_\infty$, meaning that the constant k_1 in (4.11) is simply the prefactor in the leading-order far-field behaviour of $f(\eta)$. This constant can be obtained realizing that, at the initial time $t \rightarrow t_*$, the solution must converge to a single Dirac distribution of surfactant with mass M_0 centred at x_* , and with an interfacial velocity that must be the Hilbert transform of that Dirac distribution. This can be stated mathematically as

$$A|t - t_*|^{-1/2}f(\eta) \sim \mathcal{H}[M_0\delta(x - x_*)] + iM_0\delta(x - x_*) \quad \text{as } t \rightarrow t_*. \tag{4.12}$$

Using the linearity of the Hilbert transform, the fact that $\mathcal{H}[\delta(x)] = (\pi x)^{-1}$ (King 2009b) and the rescaling property $\delta(Kx) = \delta(x)/K$ of the Dirac distribution, we obtain

$$A|t - t_*|^{-1/2}f(\eta) \sim \frac{M_0}{A}|t - t_*|^{-1/2} \left[\frac{1}{\pi\eta} + i\delta(\eta) \right] \quad \text{as } \eta \rightarrow \infty, \tag{4.13}$$

and, since we had chosen $A = \sqrt{2/Pe_s}$ in § 2.2, this means that

$$f(\eta) \sim \frac{M_0Pe_s}{2\pi} \eta^{-1} \quad \text{as } \eta \rightarrow \infty. \tag{4.14}$$

Hence, the integration constant in (4.11) must be

$$k_1 = k_\infty = \frac{M_0 Pe_s}{2\pi}. \tag{4.15}$$

The ODE (4.11) can be further integrated by noting that it is a Riccati equation, which can be solved with the change of dependent variable

$$f = -\frac{1}{h} \frac{dh}{d\eta} = -\frac{d}{d\eta} \text{Log}(h), \tag{4.16}$$

with $\text{Log}(\cdot)$ the principal value of the complex logarithm. This leads to a linear equation

$$\frac{d^2 h}{d\eta^2} + \eta \frac{dh}{d\eta} + k_1 h = 0. \tag{4.17}$$

Note the analogy between the Cole–Hopf transformation used to linearize the Burgers equation directly (Crowdy 2021*b*; Bickel & Detcheverry 2022) and the change of variables (4.16) to linearize the similarity ODE (4.11). The solution to (4.17) is

$$h(\eta) = k_2 {}_1F_1\left(\frac{k_1}{2}; \frac{1}{2}; -\frac{\eta^2}{2}\right) + k_3 \eta {}_1F_1\left(\frac{1}{2} + \frac{k_1}{2}; \frac{3}{2}; -\frac{\eta^2}{2}\right), \tag{4.18}$$

where ${}_1F_1(a; b; z)$ is Kummer’s confluent hypergeometric function (Olver *et al.* 2010) and k_2, k_3 are complex integration constants. Since, as evidenced by the change of variables (4.16), the solution $f(\eta)$ is independent of any rescalings of $h(\eta)$ with a complex constant, we can set $k_3 = 1$ without any loss of generality. The remaining constant k_2 indicates the value of the concentration C at the origin, since

$$f(0) = -\frac{1}{h(0)} \left. \frac{dh}{d\eta} \right|_{\eta=0} = -\frac{1}{k_2}, \tag{4.19}$$

which highlights that k_2 must be imaginary with $\text{Im}[k_2] > 0$. The value of k_2 can be obtained imposing the integral constraint given by (4.3), namely

$$\int_{-\infty}^{\infty} f \, d\eta = -\int_{-\infty}^{\infty} \frac{d}{d\eta} \text{Log}(h) \, d\eta = i \frac{M_0 Pe_s}{2}, \tag{4.20}$$

which can be simplified as

$$\lim_{\eta \rightarrow \infty} [\text{Log}(h(\eta)) - \text{Log}(h(-\eta))] = -i \frac{M_0 Pe_s}{2}. \tag{4.21}$$

Since k_2 is imaginary, k_1 and k_3 are real, and the hypergeometric functions in (4.18) are a function only of η^2 , we can conclude that the parity of h must be $h(-\eta) = \bar{h}(\eta)$. Using this identity, and splitting $\text{Log}(z) = \ln|z| + i\text{Arg}(z)$, we get

$$\lim_{\eta \rightarrow \infty} \text{Arg}(h(\eta)) = -\frac{M_0 Pe_s}{4} \pm \frac{\pi}{2}, \tag{4.22}$$

which, after considering the far-field behaviour of ${}_1F_1(a; b; z)$ (Olver *et al.* 2010) and the fact that $k_1 = M_0 Pe_s / (2\pi)$, leads to

$$k_2 = i \frac{\sqrt{2}}{2} \frac{\Gamma\left(\frac{M_0 Pe_s}{4\pi}\right)}{\Gamma\left(\frac{1}{2} + \frac{M_0 Pe_s}{4\pi}\right)}, \tag{4.23}$$

where $\Gamma(\cdot)$ is the gamma function and should not be confused with the surfactant concentration Γ , which is italicized throughout the paper. Undoing the change of variables

(4.16), the final form of the similarity solution is

$$f(\eta) = \frac{-6\Gamma\left(\frac{1}{2} + \zeta\right) {}_1F_1\left(\frac{1}{2} + \zeta; \frac{3}{2}; -\frac{\eta^2}{2}\right) + 6\sqrt{2}i\eta\Gamma(1 + \zeta) {}_1F_1\left(1 + \zeta; \frac{3}{2}; -\frac{\eta^2}{2}\right) + 4\eta^2\Gamma\left(\frac{3}{2} + \zeta\right) {}_1F_1\left(\frac{3}{2} + \zeta; \frac{5}{2}; -\frac{\eta^2}{2}\right)}{3\sqrt{2}i\Gamma(\zeta) {}_1F_1\left(\zeta; \frac{1}{2}; -\frac{\eta^2}{2}\right) + 6\eta\Gamma\left(\frac{1}{2} + \zeta\right) {}_1F_1\left(\frac{1}{2} + \zeta; \frac{3}{2}; -\frac{\eta^2}{2}\right)}, \tag{4.24a}$$

where we have defined

$$\zeta := \frac{M_0 Pe_s}{4\pi}. \tag{4.24b}$$

The solution given by (4.24) is equivalent to the fundamental solution derived by Bickel & Detcheverry (2022) using the Cole–Hopf transformation with a Dirac distribution as the initial condition. Figure 4 displays an initially rectangular pulse of surfactant spreading following Burgers equation (2.18a), for different values of the surface Péclet number. When advection is negligible and $Pe_s \ll 1$, the solution quickly becomes Gaussian in shape, converging towards the fundamental solution of the (linear) diffusion equation. This occurs on times of order $t = O(Pe_s)$, since at small Pe_s the dominant balance in (2.18a) modifies the characteristic time scale, which we had assumed to be set by advection in §2. As Pe_s increases and reaches an advection-dominated regime $Pe_s \gg 1$, the solution changes shape, resembling the semicircular surfactant profile of the purely advective solution (4.6) of the previous subsection.

5. Filling solutions

In the case of filling solutions, sketched in figure 1(b), there is no conserved mass of surfactant since the integral of $\Gamma_0(x)$ diverges as $\Gamma_0 \rightarrow 1$ in the far field. This leads to self-similar solutions of the second kind (Barenblatt 1996), where the exponent β cannot be determined from dimensional considerations, but is instead given by the stability criteria presented in §3.2. Furthermore, the scaling constant A is in this case dependent on the local properties of initial conditions, and can only be either computed numerically or calculated if a full solution $\psi(x, t)$ to (2.19) can be obtained explicitly.

The four filling solutions identified in §3 hold only locally, either before or after a reference ‘closure’ time t_* at which the derivative of the solution is singular. This singular behaviour has only been observed (Thess *et al.* 1997; Crowdy 2021b; Bickel & Detcheverry 2022) when the initial distribution of surfactant is zero $\Gamma_0(x) = 0$ somewhere along the real line. This fact allows us to calculate, using the method of characteristics, the time t_* , position x_* , and velocity u_* of the singular point *a priori* from the initial surfactant profile $\Gamma_0(x)$, as we illustrate in Appendix D. While symmetric surfactant profiles result in a static singularity $u_* = 0$ (as in Thess *et al.* 1997; Crowdy 2021b; Bickel & Detcheverry 2022), note that the (constant) velocity of the moving point at which the singularity develops can in general be non-zero for asymmetric profiles.

The method of characteristics can similarly be used to illustrate which initial conditions are classified as ‘dimples’, leading to $\beta = 2$, and which ones to ‘holes’, resulting in $\beta = 3/2$. As mentioned in §3.2, the key distinction between initial profiles $\Gamma_0(x)$ that lead to one or the other similarity solution is the second derivative of the solution at the singularity, which we calculate in a frame of reference moving with the singular point. To that end, we first define the position of the singular point as $x_s(t) := x_* - u_*(t_* - t)$. Then, we use the method of characteristics to obtain $\partial_{xx}\psi(x, t)$, which is given in (D3),

Self-similarity in unbounded viscous Marangoni flows

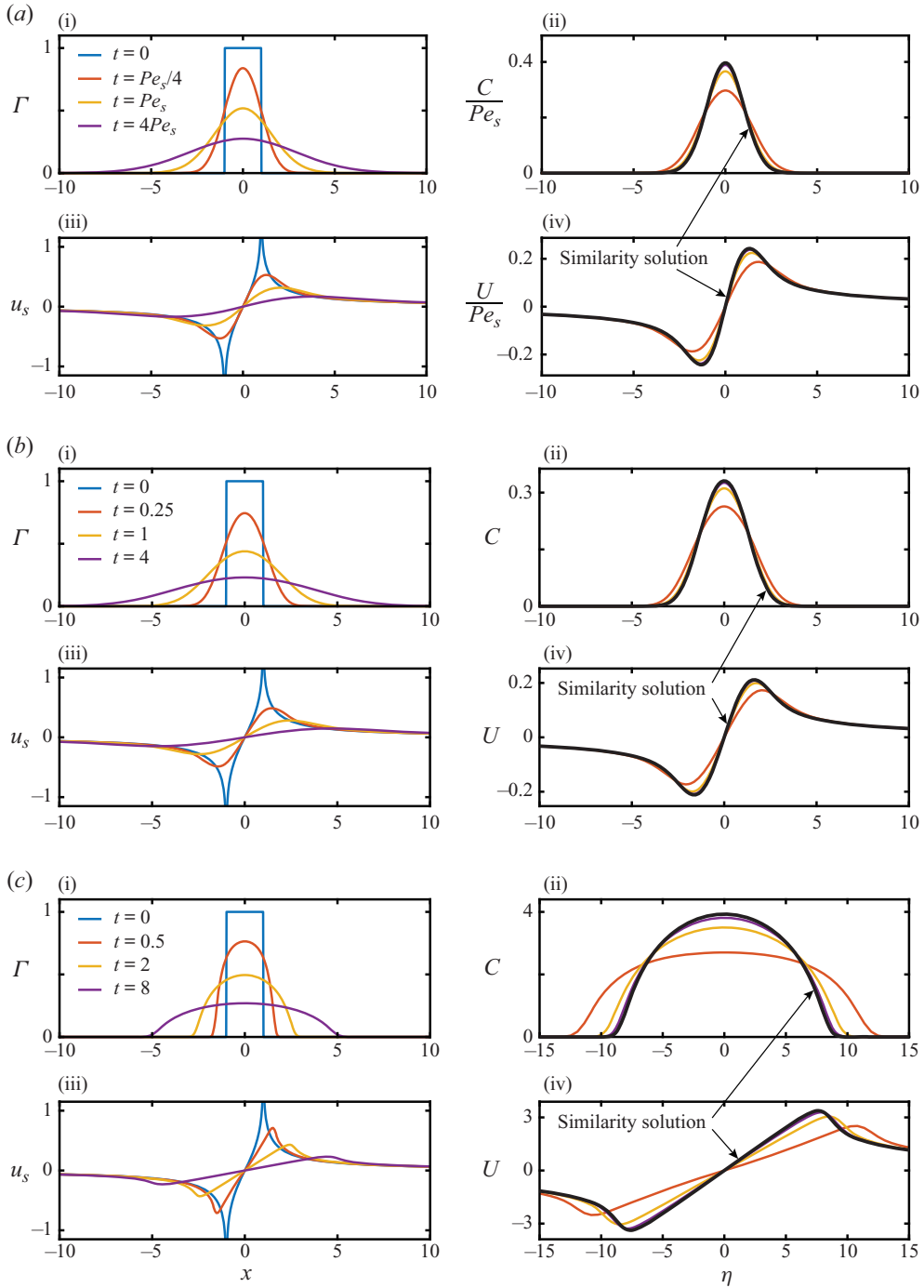


Figure 4. Spreading solutions for an initially rectangular pulse of surfactant, with a functional form given in Appendix E, for (a) $Pe_s = 1/50$, (b) $Pe_s = 1$ and (c) $Pe_s = 50$. For each example, panels (a i,iii,b i,iii,c i,iii) show the concentration $\Gamma(x, t)$ and interfacial velocity $u_s(x, t)$ obtained through the exact solution of (2.18), while panels (a ii,iv,b ii,iv,c ii,iv) show the same data rescaled in similarity variables (colour curves), superimposed on the similarity solution (4.24) (black curves) valid at long times $t \gg 1$. In all examples, $x_* = t_* = 0$.

and particularize it at $x_s(t)$ to obtain

$$\frac{\partial^2 \psi}{\partial x^2}(x_s(t), t) = \frac{\psi_0''(x_* - t_* u_*)}{(1 + t \psi_0'(x_* - t_* u_*))^3}. \tag{5.1}$$

In the case of real solutions, it can be shown that $\psi_0''(x_* - t_* u_*) = 0$ (see Appendix D), and therefore $\partial_{xx} \psi = 0$ for all times at the (moving) point of the shock. However, complex solutions can lead to either $\psi_0''(x_* - t_* u_*) \neq 0$, in which case we define the initial distribution $\Gamma_0(x)$ as a ‘dimple’, or to $\psi_0''(x_* - t_* u_*) = 0$, in which case we define it as a ‘hole.’ Each of these two cases lead to a different similarity solution and are therefore treated separately in the next two subsections.

5.1. Dimple solutions

The first dimple distribution we consider is $\Gamma_0(x) = x^2/(1 + x^2)$ (which we call the ‘Cauchy dimple’) since it has already been studied by Crowdy (2021b) and Bickel & Detcheverry (2022). It has a quadratic minimum $\Gamma_0(x) \sim x^2$ around $x = 0$ and, since it is a symmetric distribution, it follows from the method of characteristics (see Appendix D) that $u_* = x_* = 0$ and $t_* = 1$. The exact evolution of a Cauchy dimple is displayed in figure 5(a i,iv), with the surfactant concentration reaching a cusp-like singularity at t_* and x_* . Figures 5(b i,iv) and 5(c i,iv) displays the evolution of other profiles $\Gamma_0(x)$ with different functional forms (detailed in Appendix E), but always with a quadratic minimum to ensure that they display the same similarity behaviour. Self-similarity appears locally, for positions and times close enough to x_* and t_* , respectively. As discussed in § 3.2, the self-similar solution that appears prior to t_* is dubbed the ‘closure’ solution, since here the concentration remains zero $\Gamma(x_*, t) = 0$ at all times. After the dimple ‘closes’ at t_* , a different ‘levelling’ solution appears, whereby the concentration starts levelling towards the final steady distribution $\Gamma(x, t) = 1$.

It is shown in § 3.2 that the similarity exponent for dimple solutions is $\beta = 2$, which can be substituted in the implicit similarity solution (3.2) to yield

$$\text{sgn}(\eta) k_{\pm} f^2 + f - \eta = 0. \tag{5.2}$$

Solutions to (5.2) represent both (pre-singularity) closure solutions and (post-singularity) levelling solutions, which have expansions around $\eta = 0$ (table 2) given by $f(\eta) \sim \eta + iK\eta^2$ and $f(\eta) \sim iK - \eta$, respectively. Both of these expansions lead to imaginary constants k_{\pm} when introduced in (5.2). This means that, due to the symmetry condition $k_- = \bar{k}_+$ (3.3), we can consider a single constant $k = k_+ = -k_- = \text{sgn}(\eta) k_{\pm}$. Solving (5.2),

$$f(\eta) = \frac{-1 \pm \sqrt{1 + 4k\eta}}{2k}. \tag{5.3}$$

For the levelling solution, we expect $\psi(x_*, t)$, and thus $f(0)$, to be non-zero, which leads us to choose the minus sign in (5.3). This sign choice must be valid for all η since a change from $-$ to $+$ requires the square root to be zero to maintain a continuous solution, while the radicand $1 + 4k\eta$ can never be zero with k imaginary. We also fix $k = i$ so that $f(0) = i$

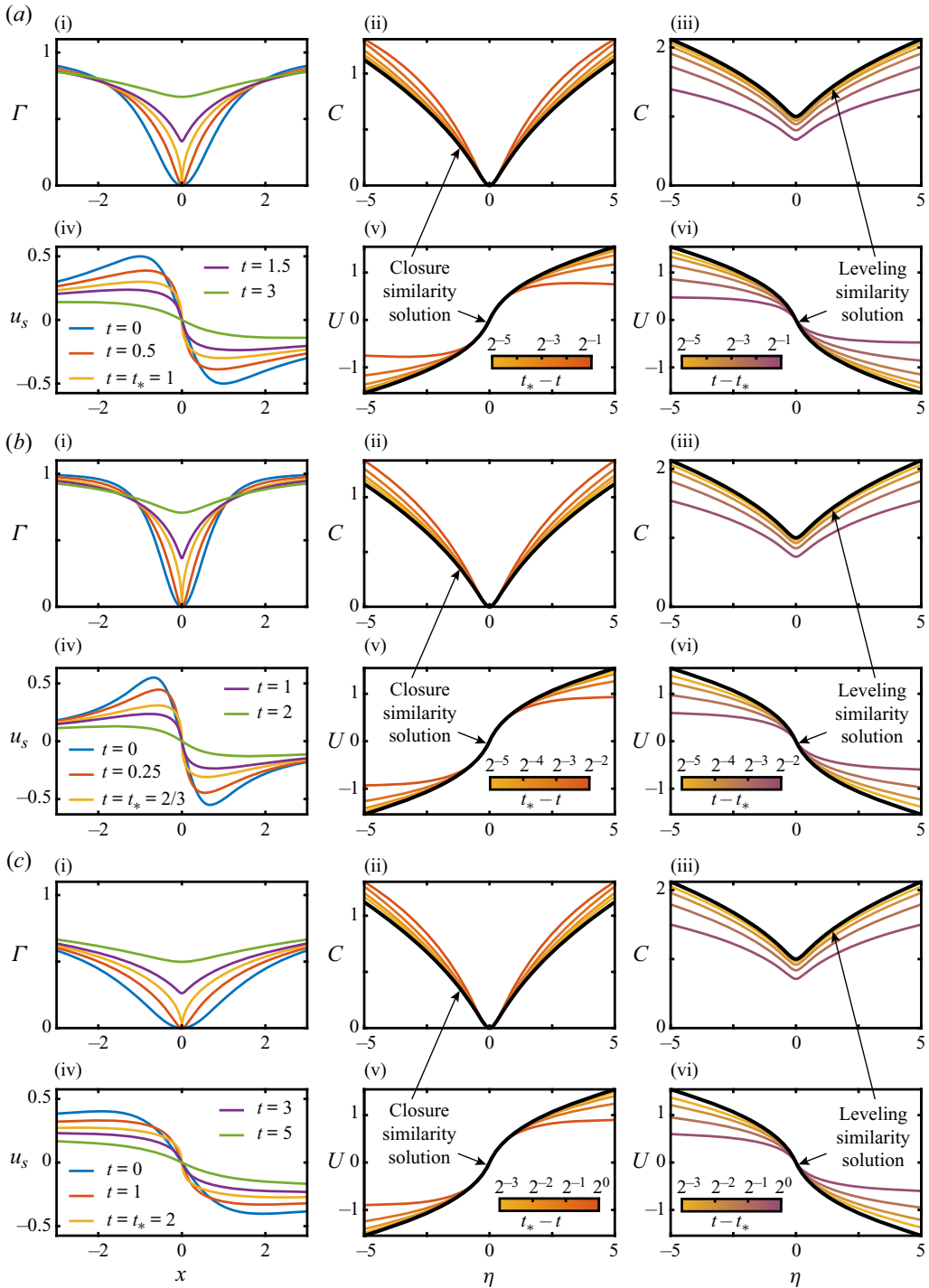


Figure 5. Filling solutions with $Pe_s^{-1} = 0$, for initial ‘dimple’ distributions of surfactant given by (a) a Cauchy dimple, (b) a squared Cauchy dimple and (c) an arctangent dimple, with their functional forms given in Appendix E. For each example, panels (a i, iv, b i, iv, c i, iv) show the concentration $\Gamma(x, t)$ and interfacial velocity $u_s(x, t)$ obtained through the exact solution of (2.19). Panels (a ii, v, b ii, v, c ii, v) and (a iii, vi, b iii, vi, c iii, vi) show exact solutions rescaled in similarity variables (colour curves), superimposed on the closure (5.7) and levelling (5.5) similarity solutions (black curves) valid prior and subsequent to the singularity, respectively. In all examples, $x_* = 0$.

(or, equivalently, $C(0) = 1$). The dimple levelling solution is then

$$f(\eta) = \frac{i}{2} \left(\sqrt{1 + 4i\eta} + 1 \right), \tag{5.4}$$

which can alternatively be decomposed into its real and imaginary parts using the relation $\sqrt{z} = \sqrt{(|z| + \text{Re}[z])/2} + i \text{sgn}(\text{Im}[z]) \sqrt{(|z| - \text{Re}[z])/2}$, leading to

$$C(\eta) = \frac{1}{2} \left(\sqrt{\frac{1}{2} \left[\sqrt{1 + 16\eta^2} + 1 \right]} + 1 \right), \tag{5.5a}$$

$$U(\eta) = -\frac{1}{2} \text{sgn}(\eta) \sqrt{\frac{1}{2} \left[\sqrt{1 + 16\eta^2} - 1 \right]}. \tag{5.5b}$$

We note that (5.5) leads to $C(\eta) \sim (\sqrt{2}/2) |\eta|^{1/2}$ and $U(\eta) \sim -\text{sgn}(\eta) (\sqrt{2}/2) |\eta|^{1/2}$ as $|\eta| \rightarrow \infty$, compatible with the far field condition (2.26).

For the closure solution, the choice in (5.3) must be the plus sign such that $f(0) = 0$. In the absence of an obvious choice for an integration constant k (since $U(0) = C(0) = 0$), we fix its value so that the far-field behaviour of the closure solution is equivalent to that of the levelling solution (5.5). In other words, we require $C(\eta) \sim (\sqrt{2}/2) |\eta|^{1/2}$ and $U(\eta) \sim \text{sgn}(\eta) (\sqrt{2}/2) |\eta|^{1/2}$ as $|\eta| \rightarrow \infty$, where the sign change in $U(\eta)$ is due to the reversal in the sign of x between the definitions of the similarity variable (2.22a) and (2.22b) for each solution. This leads to $f(\eta) \sim e^{i\pi/4} \eta^{1/2}$ as $\eta \rightarrow \infty$, which introduced in (5.2) results in $k = -i$. The final form of the dimple closure solution is then

$$f(\eta) = \frac{i}{2} \left(\sqrt{1 - 4i\eta} - 1 \right), \tag{5.6}$$

from which we obtain

$$C(\eta) = \frac{1}{2} \left(\sqrt{\frac{1}{2} \left[\sqrt{1 + 16\eta^2} + 1 \right]} - 1 \right), \tag{5.7a}$$

$$U(\eta) = \frac{1}{2} \text{sgn}(\eta) \sqrt{\frac{1}{2} \left[\sqrt{1 + 16\eta^2} - 1 \right]}. \tag{5.7b}$$

The choice of (5.4) and (5.6) having an equivalent far-field behaviour ensures that the multiplicative constant A in the similarity formulation (2.20) is the same for both the closure and the levelling solutions. This fact simplifies calculations, since it then suffices to compute A for only one of the two solutions.

Figure 5(a ii, v, b ii, v, c ii, v) shows how the exact solutions converge to the closure self-similar profiles given by (5.6) before the singularity, for the three distinct initial profiles $\Gamma_0(x)$ considered. Likewise, figure 5(a iii, vi, b iii, vi, c iii, vi) illustrates that exact solutions converge to the levelling solution (5.4) after the singularity. Since the similarity solutions are only valid locally, the agreement between the rescaled profiles is always improved as $t \rightarrow t_*$ or as $x \rightarrow x_*$.

5.2. Hole solutions

Contrary to dimples, hole similarity solutions (with $\beta = 3/2$) had not yet been identified for the complex inviscid Burgers equation (2.19a). One of the simplest examples of a

distribution of surfactant that satisfies this condition is a ‘rectangular hole’ with $\Gamma_0(x) = H(|x| - 1)$, where $H(x)$ is the Heaviside step function, which we illustrate in figure 6(a). For this case, the initial surfactant profile is even and therefore its Hilbert transform $u_{s0}(x) = \mathcal{H}[\Gamma_0(x)]$ is odd, which implies (see Appendix D) that the position of the singularity is $x_* = 0$, its velocity $u_* = 0$, and the closure time $t_* = \pi/2$. One can also easily verify that $\Gamma_0''(0) = u_{s0}''(0) = 0$ and thus the condition for hole self-similar solutions $\psi_0''(x_* - u_*t_*) = \psi_0''(0) = 0$ is satisfied. Figure 6(a) depicts the exact evolution of the rectangular hole according to the inviscid Burgers equation (2.19a). As for the case of dimples, the distribution first goes through a ‘closure’ phase where surfactant is advected inwards but remains $\Gamma(0, t) = 0$ at the origin. However, figure 6(a) also shows that the self-similar dynamics before the closure time t_* must be different from that of the dimple, since the solution retains a finite interval around $x_* = 0$ where the concentration remains zero. After $t_* = \pi/2$, the concentration at the origin starts ‘levelling’, with $\Gamma(0, t) > 0$, until the profile reaches a homogeneous distribution $\Gamma(x, t) = 1$ as $t \rightarrow \infty$.

In this case, the self-similar solutions can also be obtained in closed form by substituting $\beta = 3/2$ in the implicit solution given by (3.2), which leads to

$$k_{\pm}f^3 + f - \eta = 0. \tag{5.8}$$

Substituting the expansions around $\eta = 0$ found in table 2 for the closure ($f \sim \eta + K\eta^3$) and levelling solutions ($f \sim -iK - \eta/2$) into (5.8) leads to real constants k_{\pm} . Combined with the symmetry condition (3.3), this indicates that for either solution we can consider a single constant $k = k_- = k_+$, as in the case of spreading pulse solutions of § 4.1.

We first solve (5.8) for the case of the (post-singularity) levelling solution. We again choose to fix $f(0) = i$ or, equivalently, $C(0) = 1$, which results in $k = 1$. The discriminant of the cubic (5.8) is then $-4 - 27\eta^2$, which is negative for any η . This implies that (5.8), for any given value of η , has one real and two complex conjugate solutions that can be obtained using standard methods for solving cubic equations (Cox 2012). Choosing the complex solution with a positive imaginary part results in the hole levelling solution

$$f(\eta) = e^{i\pi/3} \sqrt[3]{\frac{1}{2} \left[\sqrt{\eta^2 + \frac{4}{27}} - \eta \right]} + e^{2i\pi/3} \sqrt[3]{\frac{1}{2} \left[\sqrt{\eta^2 + \frac{4}{27}} + \eta \right]}. \tag{5.9}$$

Furthermore, since the arguments of the two cubic roots in (5.9) are always real and positive, it is straightforward to decompose the expression into

$$C(\eta) = \frac{\sqrt{3}}{2} \left(\sqrt[3]{\frac{1}{2} \left[\sqrt{\eta^2 + \frac{4}{27}} - \eta \right]} + \sqrt[3]{\frac{1}{2} \left[\sqrt{\eta^2 + \frac{4}{27}} + \eta \right]} \right), \tag{5.10a}$$

$$U(\eta) = \frac{1}{2} \left(\sqrt[3]{\frac{1}{2} \left[\sqrt{\eta^2 + \frac{4}{27}} - \eta \right]} - \sqrt[3]{\frac{1}{2} \left[\sqrt{\eta^2 + \frac{4}{27}} + \eta \right]} \right), \tag{5.10b}$$

where the far-field behaviour $|\eta| \rightarrow \infty$ is in this case given by $C(\eta) \sim (\sqrt{3}/2)|\eta|^{1/3}$ and $U(\eta) \sim -\text{sgn}(\eta) (1/2) |\eta|^{1/3}$.

In the case of the closure solution, we again choose the integration constant such that its far field is equivalent to that of the levelling solution, which requires $k = -1$. As in the case of dimples, this choice of far field ensures that the scaling constant A in the

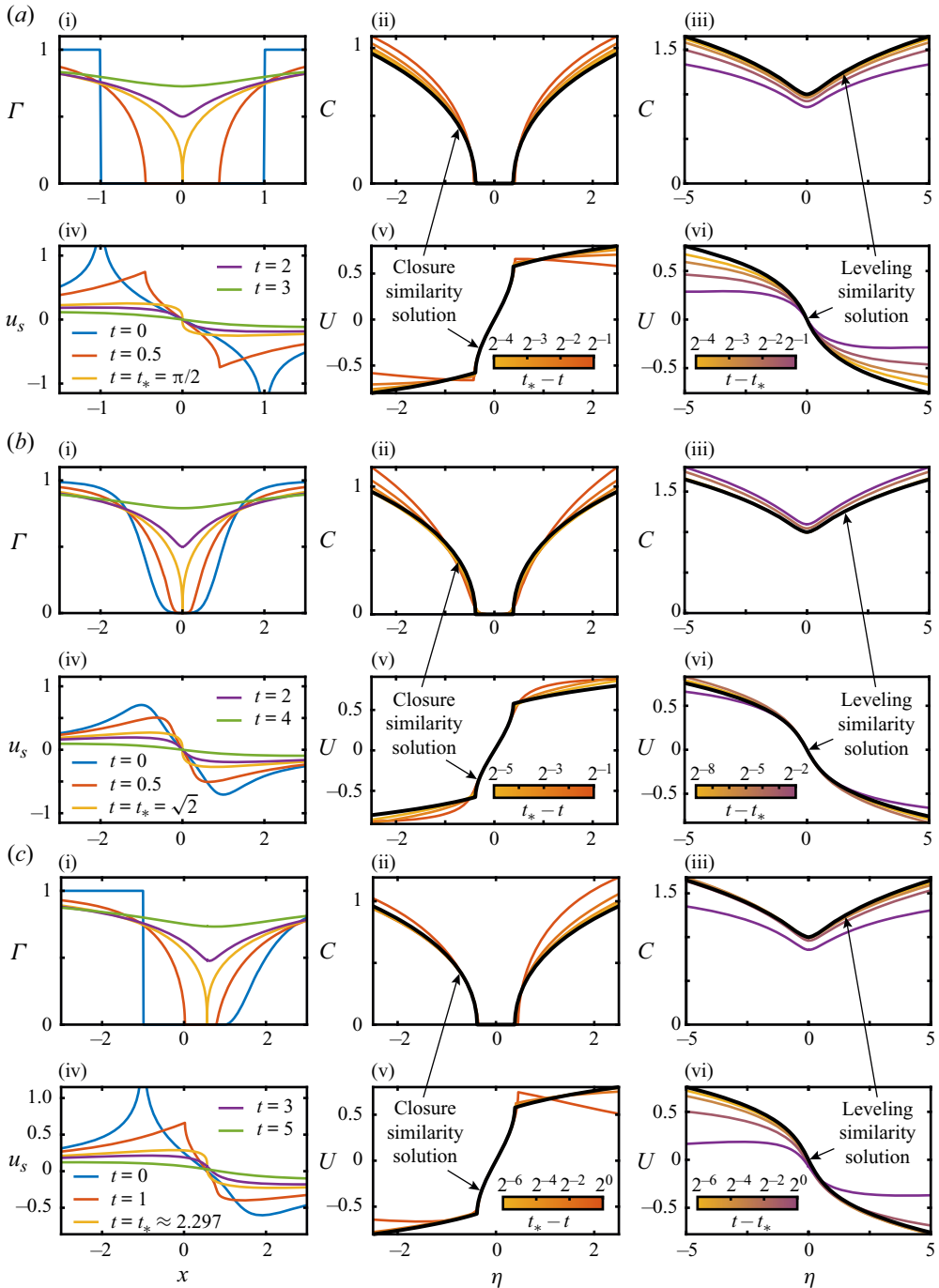


Figure 6. Filling solutions with $Pe_s^{-1} = 0$, for initial ‘hole’ distributions of surfactant given by (a) a rectangular hole, (b) a quartic hole and (c) an asymmetric hole, with their functional forms given in Appendix E. For each example, panels (a i,iv,b i,iv,c i,iv) show the concentration $\Gamma(x, t)$ and interfacial velocity $u_s(x, t)$ obtained through the exact solution of (2.19). Panels (a ii,v,b ii,v,c ii,v) and (a iii,vi,b iii,vi,c iii,vi) show exact solutions rescaled in similarity variables (colour curves), superimposed on the closure (5.13) and levelling (5.10) similarity solutions (black curves) valid prior and subsequent to the singularity, respectively. The asymmetric hole (c) has $x_* \approx 0.562$, otherwise $x_* = 0$.

similarity formulation (2.20) is the same for both closure and levelling. The discriminant of (5.8) is then $4 - 27\eta^2$, which indicates that its three solutions are real for $|\eta| \leq \sqrt{4/27} = 2\sqrt{3}/9$, whereas for $|\eta| \geq 2\sqrt{3}/9$ there is one real and two complex conjugate solutions. The only way to ensure a continuous solution with $C(\eta) > 0$ is to define $f(\eta)$ piecewise, with one of the three solutions of the cubic valid for $\eta \leq -2\sqrt{3}/9$, and another one valid for $\eta \geq -2\sqrt{3}/9$. Such a solution is

$$f(\eta) = \begin{cases} e^{i\pi/3} \left(\sqrt[3]{-\frac{1}{2} \left[\sqrt{\eta^2 - \frac{4}{27}} - \eta \right]} - \sqrt[3]{-\frac{1}{2} \left[\sqrt{\eta^2 - \frac{4}{27}} + \eta \right]} \right), & \text{if } \eta \leq -\frac{2\sqrt{3}}{9}, \\ e^{i\pi/3} \left(\sqrt[3]{\frac{1}{2} \left[\sqrt{\eta^2 - \frac{4}{27}} + \eta \right]} - \sqrt[3]{\frac{1}{2} \left[\sqrt{\eta^2 - \frac{4}{27}} - \eta \right]} \right), & \text{if } \eta \geq -\frac{2\sqrt{3}}{9}, \end{cases} \tag{5.11}$$

which can be expressed more compactly as

$$f(\eta) = e^{i\pi/3} \left(\sqrt[3]{\frac{1}{2} \left[\sqrt{\eta + \frac{2\sqrt{3}}{9} \sqrt{\eta - \frac{2\sqrt{3}}{9}} + \eta} \right]} - \sqrt[3]{\frac{1}{2} \left[\sqrt{\eta + \frac{2\sqrt{3}}{9} \sqrt{\eta - \frac{2\sqrt{3}}{9}} - \eta} \right]} \right). \tag{5.12}$$

For $|\eta| \geq 2\sqrt{3}/9$, the argument of the cubic roots in (5.12) is always real, leading to a straightforward decomposition into real and imaginary parts. However, in the case of $|\eta| \leq 2\sqrt{3}/9$, the real and imaginary parts of the solution can only be obtained through the trigonometric solution of the cubic (Cox 2012). In summary, the final form of the similarity solutions $C(\eta)$ and $U(\eta)$ is

$$C(\eta) = \begin{cases} 0 & \text{for } |\eta| \leq \frac{2\sqrt{3}}{9}, \\ \frac{\sqrt{3}}{2} \left(\sqrt[3]{\frac{1}{2} \left[|\eta| + \sqrt{\eta^2 - \frac{4}{27}} \right]} - \sqrt[3]{\frac{1}{2} \left[|\eta| - \sqrt{\eta^2 - \frac{4}{27}} \right]} \right) & \text{for } |\eta| \geq \frac{2\sqrt{3}}{9}, \end{cases} \tag{5.13a}$$

$$U(\eta) = \begin{cases} \frac{2\sqrt{3}}{3} \sin \left[\frac{1}{3} \arcsin \left(\frac{3\sqrt{3}}{2} \eta \right) \right], & \text{for } |\eta| \leq \frac{2\sqrt{3}}{9}, \\ \frac{1}{2} \operatorname{sgn}(\eta) \left(\sqrt[3]{\frac{1}{2} \left[|\eta| + \sqrt{\eta^2 - \frac{4}{27}} \right]} + \sqrt[3]{\frac{1}{2} \left[|\eta| - \sqrt{\eta^2 - \frac{4}{27}} \right]} \right), & \text{for } |\eta| \geq \frac{2\sqrt{3}}{9}, \end{cases} \tag{5.13b}$$

where we can verify that its far field as $|\eta| \rightarrow \infty$, which is given by $C(\eta) \sim (\sqrt{3}/2)|\eta|^{1/3}$ and $U(\eta) \sim \operatorname{sgn}(\eta) (1/2)|\eta|^{1/3}$, is equivalent to that of the levelling solution.

Figures 6(a ii,v) and 6(a iii,vi) show that the exact solution, when appropriately rescaled using (2.20), converges to the closure solution (5.13) before t_* and to the levelling solution (5.10) after t_* . Other initial surfactant profiles also lead to these similarity solutions, as long as the condition $\psi_0''(x_* - t_*u_*) = 0$ is met. It is worth noting that the initial surfactant

distribution does not need to be zero at a finite interval to tend to a self-similar solution for a hole, as exemplified by the ‘quartic hole’ initial condition $\Gamma_0(x) = x^4/(1 + x^4)$, whose evolution is displayed in figure 6(b). This initial profile also has even symmetry, leading to $x_* = 0$, $u_* = 0$, and $t_* = \sqrt{2}$ (see Appendix D), but its initial concentration is zero only at the origin $x_* = 0$. Regardless, since $\psi_0''(x_* - u_*t_*) = \psi_0''(0) = 0$, the profiles evolve towards the closure solution (5.12) for $t < t_*$ (figure 6b ii,v) and towards the levelling solution (5.9) for $t > t_*$ (figure 6b iii,vi). Even though $\Gamma_0(x)$ is zero at a single point, the concentration ‘flattens’ as $t \rightarrow t_*$ to converge towards a solution that is zero at a finite interval.

The last example illustrated in figure 6(c) is an asymmetric initial condition. For this case, we have that $x_* \neq 0$ and $u_* \neq 0$, although their values can still be calculated from the method of characteristics, as detailed in Appendix D. The self-similar dynamics is still governed by the solutions (5.12) and (5.9) although, since the point of the singularity moves with $u_* \neq 0$, the similarity variable must account for a frame of reference moving with the singular point. This leads to a more general similarity ansatz

$$\psi(x, t) = u_* + A|t - t_*|^{\beta-1}f(\eta), \tag{5.14a}$$

$$\eta = \text{sgn}(t - t_*) \frac{x - [x_* + u_*(t - t_*)]}{A|t - t_*|^\beta}. \tag{5.14b}$$

Equation (5.14) accounts for the moving singular point, whose position is $x_s(t) = x_* + u_*(t - t_*)$. Note that $x_s(t_*) = x_*$, whereas $x_s(0) = x_* - u_*t_*$, which is the departure position of the moving singular point.

6. Conclusions

Quantitatively describing Marangoni flows induced by surfactant is a central problem in interfacial fluid dynamics, due to their prevalence in environmentally and industrially relevant multiphase flows. Motivated by recent theoretical progress, we have investigated the two-dimensional spreading problem for a deep, viscous subphase in terms of its self-similarity. The analysis reveals a rich structure with six distinct similarity solutions and three different exponents β , listed in table 4, all of which can be obtained in closed form.

In § 4, we derive one similarity solution without diffusion ($Pe_s^{-1} = 0$) and another with diffusion ($Pe_s^{-1} > 0$) for the case of pulses of surfactant, both of which are valid at long times $t \gg 1$. The solution with $Pe_s^{-1} = 0$ is in fact only valid for times up to $1 \ll t \ll Pe_s$, since at $t = O(Pe_s)$ the interfacial velocity is expected to become small enough for diffusion to be comparable to advection. These two spreading solutions are equivalent to the ones previously identified by Thess (1996) and Bickel & Detcheverry (2022), respectively, through different methods. In addition to their derivation, we have also shown (Appendix C) how to calculate the centre of mass x_* around which these solutions appear, something particularly useful when the initial surfactant distribution is asymmetric or the combination of several pulses. Since their similarity exponent is $\beta = 1/2$, these pulse solutions are analogous to a diffusive process where the surfactant peak decreases as $\Gamma \propto t^{-1/2}$, and its front spreads as $x_f \propto t^{1/2}$. These two solutions can therefore be used to obtain effective surfactant diffusivities resulting from the Marangoni flow, as detailed by Bickel & Detcheverry (2022). We also note that the solutions $N \rightarrow O$ in the phase plane (figure 2) that have $1/2 < \beta < 1$ are also spreading and, in principle, physically admissible in terms of their stability (§ 3.2). Therefore, we postulate that surfactant pulses

Name	Pe_s^{-1}	Kind	Validity	Exponent β	Similarity variable η	Solution $f(\eta)$
Pulse	0	First	$t \gg 1$	1/2	$\frac{x - x_*}{\left(\frac{M_0}{\pi} t\right)^{1/2}}$	(4.6)
Pulse	> 0	First	$t \gg 1$	1/2	$\frac{x - x_*}{\left(\frac{2}{Pe_s} t\right)^{1/2}}$	(4.24)
Dimple closure	0	Second	$t \lesssim t_*$	2	$\frac{[x_* + u_*(t - t_*)] - x}{A(t_* - t)^2}$	(5.6)
Dimple levelling	0	Second	$t \gtrsim t_*$	2	$\frac{x - [x_* + u_*(t - t_*)]}{A(t - t_*)^2}$	(5.4)
Hole closure	0	Second	$t \lesssim t_*$	3/2	$\frac{[x_* + u_*(t - t_*)] - x}{A(t_* - t)^{3/2}}$	(5.12)
Hole levelling	0	Second	$t \gtrsim t_*$	3/2	$\frac{x - [x_* + u_*(t - t_*)]}{A(t - t_*)^{3/2}}$	(5.9)

Table 4. Summary of the six similarity solutions found in this study, indicating the equation number of each solution $f(\eta)$ obtained in closed form. Here, M_0 is the dimensionless surfactant mass as defined in (C2), and Pe_s is the Péclet number given by (2.17). In the case of pulses, the reference position x_* is the centre of mass of the surfactant distribution given by (4.10), and in the case of dimples and holes x_* is the ‘closure position’ at which the solution has a weak singularity, which can be calculated *a priori* from the initial conditions as described in Appendix D. The parameters t_* and u_* are the closure time and instantaneous velocity of the singular point, respectively, and can also be calculated using Appendix D. For solutions of the second kind, the constant A depends on local properties of the initial condition $\Gamma_0(x)$.

that decay too slowly in the far field to have a well-defined mass M_0 might display this kind of self-similar solution.

Section 5 is concerned with surfactant distributions that are locally depleted and flow inwards, for which similarity only occurs for $Pe_s^{-1} = 0$. We have provided the first derivation of two similarity solutions with $\beta = 2$ and another two with $\beta = 3/2$. Through insights provided by stability analysis (§ 3.2) and the complex method of characteristics, we have also provided a quantitative criterion to determine if a given initial surfactant profile will develop similarity with $\beta = 2$, in which case we call such profile a ‘dimple’, or with $\beta = 3/2$, in which case we call it a ‘hole.’ Aside from providing valuable information about the spatial and temporal structure of the evolution of surfactant, these solutions also allow us to calculate effective local properties of the flow. For example, from the similarity ansatz (2.20b), we can deduce that the concentration at the centreline x_* of an interfacial strip that is depleted of surfactant is

$$\Gamma(x_*, t) = \begin{cases} 0, & \text{if } 0 \leq t \leq t_*, \\ A(t - t_*), & \text{if } t \gtrsim t_*, \end{cases} \quad (6.1)$$

for dimples, while for holes

$$\Gamma(x_*, t) = \begin{cases} 0, & \text{if } 0 \leq t \leq t_*, \\ A(t - t_*)^{1/2}, & \text{if } t \gtrsim t_*, \end{cases} \quad (6.2)$$

where t_* can be obtained exactly if $\Gamma_0(x)$ is known, as detailed in Appendix D.

Since local surfactant concentrations are challenging to measure experimentally, one can also derive expressions for the centreline interfacial shear, which reads

$$\frac{\partial u_s}{\partial x}(x_*, t) = \begin{cases} \frac{1}{t_* - t} & \text{if } t \lesssim t_*, \\ \frac{1}{t - t_*} & \text{if } t \gtrsim t_*, \end{cases} \quad (6.3)$$

for dimples, and

$$\frac{\partial u_s}{\partial x}(x_*, t) = \begin{cases} \frac{1}{t_* - t} & \text{if } t \lesssim t_*, \\ \frac{1}{2(t - t_*)} & \text{if } t \gtrsim t_*, \end{cases} \quad (6.4)$$

for holes. These expressions for the interfacial shear are, in principle, obtainable by measuring the interfacial velocity field in experiments, and should be valid for times sufficiently near t_* , but not too close to the singularity for surface diffusion to locally regularize the interfacial velocity field. The expressions do not depend on any scaling constant A , and the only parameter involved, t_* , can be either calculated exactly if $\Gamma_0(x)$ is known, or measured from experimental data.

This taxonomy of self-similar solutions provides insights into the behaviour of Marangoni flows on a deep fluid subphase, in the limit of low Reynolds and capillary numbers. A natural question arises from this analysis: Given an arbitrary initial distribution of surfactant, will it always evolve to one of these similarity solutions? We expect that any profile decaying in the far field will eventually converge to ‘spreading’ similarity solutions, either with diffusion (4.24) or without it (4.6) if $Pe_s \gg 1$. This is consistent with general self-similar behaviour appearing in scale-free physical systems at long times (Barenblatt 1996), and we have observed it even with multiple surfactant pulses (see figure 3c). On the other hand, ‘filling’ self-similar solutions appear locally for depleted distributions of surfactant, but only in the absence of diffusion and if the initial concentration $\Gamma_0(x)$ is exactly zero at some point. We have conducted a preliminary comparison between the ‘hole’ and ‘dimple’ solutions and simulations in more realistic scenarios, which include small amounts of background endogenous surfactant (see Grotberg *et al.* 1995) and a finite diffusion (as also analysed by Crowdy 2021b). We found that surface diffusion, no matter how small, locally regularizes the singularities in the derivatives, but the similarity solutions still provide a good approximation of the dynamics at high $Pe_s \gg 1$. This suggests that any profile that does not decay in the far field but is locally depleted could potentially be approximated by self-similar solutions, as long as the minimum value of $\Gamma_0(x)$ and diffusion are both sufficiently low. A detailed analysis, which could perhaps be achieved perturbatively, could provide further insights into the generality of self-similar behaviour given arbitrary initial conditions. Similarly, it is worth asking if a self-similarity approach would yield similar insights into an axisymmetric geometry, since this work deals exclusively with a planar, two-dimensional domain. The axisymmetric problem has a more complicated non-local closure (Bickel & Detcheverry 2022) for which it appears that no reformulations like the Burgers equation exist, but the tools of self-similarity could still be applied for non-local problems (as in Lister & Kerr 1989, for example).

Funding. F.T.C. acknowledges support from a Distinguished Postdoctoral Fellowship from the Andlinger Center for Energy and the Environment. We thank the National Science Foundation for partial support through grant CBET 2127563.

Declaration of interests. The authors report no conflict of interest.

Author ORCIDs.

 Fernando Temprano-Coleto <https://orcid.org/0000-0002-2179-3148>;

 H.A. Stone <https://orcid.org/0000-0002-9670-0639>.

Appendix A. Construction of the phase plane

We first recast the autonomous ODE (3.1), which governs the behaviour of the complex similarity solution $f(\eta) = \eta g(\eta)$ in the limit $Pe_s^{-1} = 0$, as

$$\frac{dg}{d \ln |\eta|} = \frac{g(1-g)(\bar{g} - \beta)}{|g - \beta|^2}, \tag{A1}$$

with the overbar indicating complex conjugation. Since the right-hand side of the above ODE has a singularity at $g = \beta$, we reparametrize the equation (as in, for instance, Slim & Huppert 2004) in terms of an auxiliary variable χ , leading to

$$\frac{dg}{d\chi} = g(1-g)(\bar{g} - \beta), \tag{A2a}$$

$$\frac{d \ln |\eta|}{d\chi} = |g - \beta|^2. \tag{A2b}$$

Since, by virtue of (A2b) above, we have that $d \ln |\eta|/ d\chi \geq 0$, then integrating the system in terms of χ instead of $\ln |\eta|$ does not change the direction of trajectories in the phase space $(\text{Re}[g], \text{Im}[g])$, unlike in other more complicated systems of equations such as the one considered in Slim & Huppert (2004). The three fixed points of (A2a) are given by $g = 0$, $g = 1$ and $g = \beta$ and linearization around each of them (Strogatz 2018) reveals their type, as well as the asymptotic form of the solution around each of them (points O , P and S in table 2).

We integrate (A2) numerically using the built-in MATLAB integrator `ode15s`. The initial condition of (A2b) is chosen as $(\ln |\eta|)|_{\chi=0} = -K$, with $K \gg 1$ to represent a point close to the origin $\eta \approx 0$. The initial values of g are seeded close to the fixed points of the system such that $g(\chi = 0) = g_0 + \Delta e^{i\theta}$, with $\Delta \ll 1$ and θ real constants, and where g_0 is the value of g at each fixed point. We integrate (A2a) forward in χ if $g(\chi = 0)$ lies on an unstable direction around the fixed point, and backward in χ if $g(\chi = 0)$ lies on a stable direction. Integration proceeds until $\ln |\eta|$ reaches a target value $\ln |\eta| = K \gg 1$, denoting the far field $|\eta| \rightarrow \infty$. The resulting trajectories are shown in figure 2.

We also consider the behaviour of trajectories as $|g| \rightarrow \infty$, which can be illustrated by studying the fixed points of the dynamical system given by the reciprocals $1/\text{Re}[g] = \eta/U$ and $1/\text{Im}[g] = \eta/C$. Splitting the complex ODE (3.1) into its real and imaginary parts, and changing variables $\tilde{u} := 1/\text{Re}[g]$ and $\tilde{c} := 1/\text{Im}[g]$, we obtain the following system of ODEs:

$$\frac{d\tilde{u}}{d \ln |\eta|} = \tilde{u} \frac{[\tilde{u}^2(1 + (\beta - 1)\tilde{u}) - \tilde{c}^2(\tilde{u} - 1)(1 - \beta\tilde{u})]}{\tilde{u}^2 + \tilde{c}^2(1 - \beta\tilde{u})^2}, \tag{A3a}$$

$$\frac{d\tilde{c}}{d \ln |\eta|} = \tilde{c} \frac{[\tilde{u}^2 + \tilde{c}^2(1 - 2\beta\tilde{u} + \beta\tilde{u}^2)]}{\tilde{u}^2 + \tilde{c}^2(1 - \beta\tilde{u})^2}. \tag{A3b}$$

The fixed points of (A3) are $(\tilde{u}, \tilde{c}) = (0, 0)$, which represents $(\text{Re}[g], \text{Im}[g]) \rightarrow (\pm\infty, \pm\infty)$, and $(\tilde{u}, \tilde{c}) = ((1 - \beta)^{-1}, 0)$, which represents $(\text{Re}[g], \text{Im}[g]) \rightarrow (1 - \beta, \pm\infty)$.

Linearization around these two points leads to the rows of [table 2](#) corresponding to points *N* and *R*.

Finally, the behaviour of solutions for $\text{Re}[g] \rightarrow \pm\infty$ and $\text{Im}[g] = 0$ can only be determined by examining the dynamical system given by the reciprocal $1/\text{Re}[g] = \eta/U$, retaining the imaginary part $\text{Im}[g]$. Changing variables $\tilde{u} := 1/\text{Re}[g]$ and $\hat{c} := \text{Im}[g]$, we obtain a dynamical system given by

$$\frac{d\tilde{u}}{d \ln |\eta|} = \tilde{u} \frac{[\tilde{u}\hat{c}^2(1 + (\beta - 1)\tilde{u}) - (\tilde{u} - 1)(1 - \beta\tilde{u})]}{(1 - \beta\tilde{u})^2 + \tilde{u}^2\hat{c}^2}, \tag{A4a}$$

$$\frac{d\hat{c}}{d \ln |\eta|} = \hat{c} \frac{[1 - 2\beta\tilde{u} + \beta\tilde{u}^2 + \tilde{u}^2\hat{c}^2]}{(1 - \beta\tilde{u})^2 + \tilde{u}^2\hat{c}^2}. \tag{A4b}$$

The only fixed point of (A4) is $(\tilde{u}, \hat{c}) = (0, 0)$, which represents $(\text{Re}[g], \text{Im}[g]) \rightarrow (\pm\infty, 0)$. Linearization of (A4) around it results in the row of [table 2](#) corresponding to point *M*.

Appendix B. Interpretation of the phase plane

In order to interpret the phase plane in [figure 2](#), it is useful to note two facts about the sign of solutions. First, from the self-similar ansatz (2.21b) and the facts that $\alpha = \beta - 1$ and $A = B$, we have at the origin $x = x_*$ that $\Gamma(x_*, t) = A|t - t_*|^{\beta-1}C(0)$, illustrating that, if $C(0) > 0$, values of $0 < \beta < 1$ will result in surfactant locally decreasing in time (i.e. spreading solutions), whereas exponents $\beta > 1$ represent locally increasing surfactant (i.e. filling solutions). Consequently, solutions with $0 < \beta < 1$ must lead to a (locally) outward flow as in [figure 1\(a\)](#), with u_s positive for $x > x_*$ and u_s negative for $x < x_*$ or, in other words, $(x - x_*)u_s > 0$. On the other hand, solutions with $\beta > 1$ must lead to $(x - x_*)u_s < 0$ locally around the origin as in [figure 1\(b\)](#).

Second, physical solutions require $\Gamma(x, t) \geq 0$ and therefore also $C(\eta) \geq 0$. Since each quadrant of the phase plane has a fixed sign of $C(\eta)/\eta$ and $U(\eta)/\eta$, it then follows that each quadrant must also have a fixed sign of η and $U(\eta)$ individually. These sign restrictions lead to a unique meaning for each quadrant of the phase plane, as illustrated in [figure 7](#). For a given value of β , each quadrant must represent either a forward-time (2.22a) or backward-time (2.22b) scaling, as well as necessarily belong to either the right half of the real line (i.e. $x > x_*$), or to the left half (i.e. $x < x_*$).

Appendix C. Invariants of the problem

Direct integration of the surfactant conservation law given by (2.3) yields

$$\frac{d}{dt} \int_{-\infty}^{\infty} \Gamma \, dx + (u_s \Gamma)|_{-\infty}^{\infty} = \frac{1}{Pe_s} \left. \frac{\partial \Gamma}{\partial x} \right|_{-\infty}^{\infty}, \tag{C1}$$

and, since $u_s(x, t)$ necessarily decays and $\Gamma(x, t)$ can be at most constant in the far field,

$$\frac{d}{dt} \int_{-\infty}^{\infty} \Gamma \, dx = 0. \tag{C2}$$

Equation (C2) implies that the total mass M_0 of surfactant, as defined in (4.1), is conserved in time. This holds as long as the integral given by (4.1) exists, which is the case for initial pulses of surfactant with $\Gamma_0(x)$ decaying sufficiently quickly as $|x| \rightarrow \infty$.

Self-similarity in unbounded viscous Marangoni flows

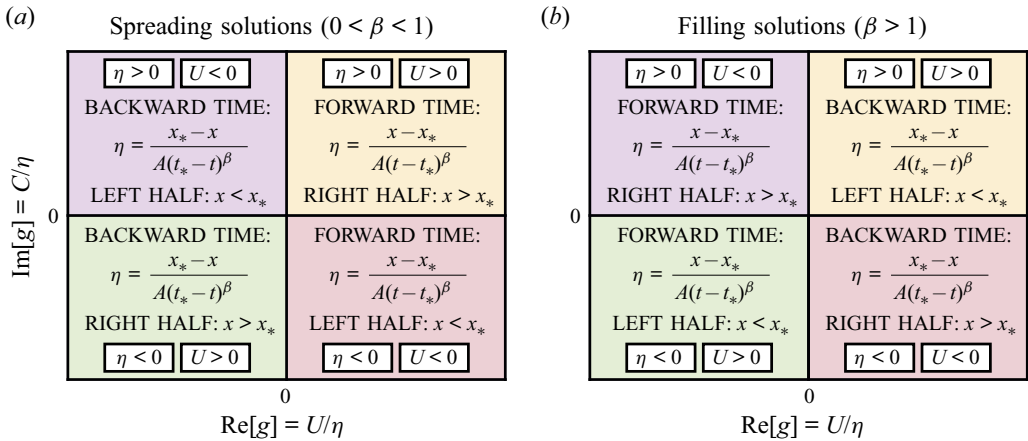


Figure 7. Physical interpretation of each quadrant of the phase plane in figure 2, for (a) spreading solutions with an outward flow (as in figure 1a), and (b) filling solutions with an inward flow (as in figure 1b). In order for the concentration $\Gamma(x, t)$ to be strictly non-negative, each quadrant must correspond to a specific definition of the similarity variable, either forward time as in (2.22a) or backward time as in (2.22b). In addition, each quadrant represents one half of the real line, either $x > x_*$ or $x < x_*$.

Furthermore, multiplying (2.3) by x and applying the chain rule, we obtain

$$\frac{\partial (x\Gamma)}{\partial t} + \frac{\partial}{\partial x} (xu_s\Gamma) - u_s\Gamma = \frac{1}{Pe_s} \left[\frac{\partial}{\partial x} \left(x \frac{\partial \Gamma}{\partial x} \right) - \frac{\partial \Gamma}{\partial x} \right], \quad (C3)$$

which, upon integration, yields

$$\frac{d}{dt} \int_{-\infty}^{\infty} x\Gamma \, dx + (xu_s\Gamma)|_{-\infty}^{\infty} - \int_{-\infty}^{\infty} u_s\Gamma \, dx = \frac{1}{Pe_s} \left[\left(x \frac{\partial \Gamma}{\partial x} \right) \Big|_{-\infty}^{\infty} - \Gamma \Big|_{-\infty}^{\infty} \right]. \quad (C4)$$

Since the far-field concentration of surfactant can be at most constant with the same values as $x \rightarrow \infty$ and as $x \rightarrow -\infty$, all the far-field flux terms in (C4) vanish as long as the product $u_s\Gamma$ decays at least as $u_s\Gamma \sim x^{-1}$ as $|x| \rightarrow \infty$. Remarkably, since in this problem $u_s = \mathcal{H}[\Gamma]$, the integral term in (C4) also vanishes due to the orthogonality condition of the Hilbert transform (King 2009a), namely

$$\int_{-\infty}^{\infty} u_s\Gamma \, dx = \int_{-\infty}^{\infty} \mathcal{H}[\Gamma]\Gamma \, dx = 0. \quad (C5)$$

All the above implies that the first moment M_1 of the surfactant distribution, as defined in (4.9), is also conserved, satisfying

$$\frac{d}{dt} \int_{-\infty}^{\infty} x\Gamma \, dx = 0, \quad (C6)$$

as long as $x\Gamma_0(x)$ decays sufficiently quickly for the above integral to exist.

Appendix D. Closure time of dimple/hole distributions

The solution of the inviscid Burgers problem (2.19) can be written implicitly using the method of characteristics (Crowdy 2021b), yielding

$$\psi(x, t) = \psi_0(x - t\psi(x, t)). \tag{D1}$$

Defining the characteristic variable $\xi(x, t) := x - t\psi(x, t)$ and differentiating (D1) yields

$$\frac{\partial \psi}{\partial x}(x, t) = \frac{\psi'_0(\xi)}{1 + t\psi'_0(\xi)}. \tag{D2}$$

Therefore, singularities in the solution derivatives occur when $1 + t_*\psi'_0(\xi_*) = 0$, for some characteristic $\xi_* = x_* - t_*\psi(x_*, t_*)$ crossing the singularity coordinate x_* at time t_* . If the solution $\psi(x, t)$ is real, the characteristic is also real, leading to the classic result (see e.g. Olver 2014) of a shock appearing at the earliest possible time $t_* = \min_{\xi}\{-1/\psi'_0(\xi)\}$, from which it follows that $\psi''_0(\xi_*) = 0$. This highlights that any given (real) initial distribution $\psi_0(x) > 0$ must have a negative slope $\psi'_0 < 0$ somewhere along the real line for a singularity to develop. We can also calculate the second derivative of the solution

$$\frac{\partial^2 \psi}{\partial x^2}(x, t) = \frac{\psi''_0(\xi)}{(1 + t\psi'_0(\xi))^3}. \tag{D3}$$

In the case of real solutions, at the point $x_s(t) := x_* - (t_* - t)\psi(x_*, t_*)$ moving with the shock, the second derivative is $\partial_{xx}\psi(x_s(t), t) = \psi''_0(\xi_*)/(1 + t\psi'_0(\xi_*))^3 = 0$, which highlights that the profile is locally linear in the moving frame of reference.

The case of complex solutions is more complicated, since the condition for a singularity to occur must be satisfied for both the real and imaginary parts of a complex-valued ξ_*

$$1 + t_*\text{Re}[\psi'_0(\xi_*)] = 0, \quad \text{Im}[\psi'_0(\xi_*)] = 0. \tag{D4}$$

Previous studies (Thess 1996; Crowdy 2021b; Bickel & Detcheverry 2022) identified that singularities develop at points where surfactant not only reaches a minimum, but also has a value of zero $\Gamma(x_*, t_*) = 0$. Building upon this observation, we limit our analysis to singularities where $\text{Im}[\psi(x_*, t_*)] = 0$, which in turn leads to a real characteristic ξ_* . In that case, we have that $\psi'_0(\xi_*) = u'_{s0}(\xi_*) + i\Gamma'_0(\xi_*)$ and the conditions (D4) for a singularity to occur are simplified, leading to

$$1 + t_*u'_{s0}(\xi_*) = 0, \quad \Gamma'_0(\xi_*) = 0. \tag{D5}$$

The closure time t_* can then be calculated as follows:

- (i) If the surfactant distribution is sufficiently smooth and zero at a single point $\Gamma_0(x_0) = 0$, then such point x_0 must be a minimum, and so conditions (D5) then lead to $x_0 = \xi_*$ and a singularity time given by

$$t_* = -\frac{1}{u'_{s0}(\xi_*)}, \text{ with } \xi_* \text{ such that } \Gamma'_0(\xi_*) = \Gamma_0(\xi_*) = 0. \tag{D6}$$

While $\Gamma'_0(\xi_*) = 0$, the second derivative could be either $\Gamma''_0(\xi_*) > 0$ in the case of a quadratic minimum or $\Gamma''_0(\xi_*) = 0$ for flatter distributions like, for instance, one with a quartic minimum. For that reason, (D6) applies for ‘dimples’, described in § 5.1, and also for some ‘holes’, such as the quartic hole described in § 5.2. In general, once t_* and ξ_* are calculated using (D6), one can retrieve the velocity of the singularity

Name	$\Gamma_0(x)$	$u_{s0}(x) = \mathcal{H}[\Gamma_0(x)]$	$\psi_0(z)$	M_0	t_*
Cauchy pulse	$\frac{1}{1+x^2}$	$\frac{x}{1+x^2}$	$\frac{1}{z-i}$	π	N/A
Rectangular pulse	$H(1- x)$	$\frac{1}{\pi} \ln \left \frac{x+1}{x-1} \right $	$\frac{1}{\pi} \text{Log} \left(\frac{z+1}{z-1} \right)$	2	N/A
Half-Cauchy pulse	$\frac{H(x)}{1+x^2}$	$\frac{\pi x + 2 \ln x }{2\pi(1+x^2)}$	$\frac{\pi(z+i) + 2\text{Log}(z)}{2\pi(1+z^2)}$	$\frac{\pi}{2}$	N/A
Quartic pulse	$\frac{1}{1+x^4}$	$\frac{x(1+x^2)}{\sqrt{2}(1+x^4)}$	$\frac{z-i\sqrt{2}}{\sqrt{2}(z^2-i\sqrt{2}z-1)}$	$\frac{\sqrt{2}\pi}{2}$	N/A
Cauchy dimple	$1 - \frac{1}{1+x^2}$	$-\frac{x}{1+x^2}$	$\frac{iz}{z-i}$	∞	1
Squared Cauchy dimple	$1 - \frac{1}{(1+x^2)^2}$	$-\frac{x(3+x^2)}{2(1+x^2)^2}$	$\frac{iz(2z-3i)}{2(z-i)^2}$	∞	$\frac{2}{3}$
Arctangent dimple	$1 - \frac{\arctan x}{x}$	$-\frac{\ln(1+x^2)}{2x}$	$i - \frac{\text{Log}(1+iz)}{z}$	∞	2
Rectangular hole	$H(x -1)$	$\frac{1}{\pi} \ln \left \frac{x-1}{x+1} \right $	$\frac{1}{\pi} \text{Log} \left(\frac{1-z}{1+z} \right)$	∞	$\frac{\pi}{2}$
Quartic hole	$1 - \frac{1}{1+x^4}$	$-\frac{x(1+x^2)}{\sqrt{2}(1+x^4)}$	$\frac{z(1+i\sqrt{2}z)}{\sqrt{2}(z^2-i\sqrt{2}z-1)}$	∞	$\sqrt{2}$

Table 5. Initial conditions $\Gamma_0(x)$ and $u_{s0}(x)$ used in the article. The fourth column lists the lower-analytic complex function $\psi_0(z)$, with $z = x + iy$, that results in $\psi_0(x) = u_{s0}(x) + i\Gamma_0(x)$ on the real axis $y = 0$. The fifth column denotes the mass of surfactant, as defined in (4.1), for the case of pulses. The last column specifies the singularity time t_* for holes or dimples, as defined in (D6) and (D7). Here, $H(x)$ denotes the Heaviside step function.

$u_* = u_{s0}(\xi_*)$ and then the actual position x_* of the singularity using $x_* = \xi_* + t_*u_*$. In the case of a symmetric surfactant distribution (as in figures 5 and 6b), the odd interfacial velocity imposes $u_* = 0$ and thus the singular point is static with $x_* = \xi_*$.

- (ii) If the initial surfactant is zero on a finite interval, then $\Gamma'_0(\xi) = \Gamma''_0(\xi) = 0$ on any point of the interval as well. This is the case for some ‘holes’ such as the rectangular hole and the asymmetric hole from § 5.2. Such distributions lead to singularities at multiple points, since the solution develops a moving front that converges inwards as in figure 6(a,c). However, the hole closure time t_* will be determined by the last instant in which a singularity occurs, so it can in this case be calculated as

$$t_* = \max_{\xi} \left\{ -\frac{1}{u'_{s0}(\xi)} \right\}, \quad \text{and} \quad \xi_* = \arg \max_{\xi} \left\{ -\frac{1}{u'_{s0}(\xi)} \right\}, \quad (D7)$$

which also implies that $u''_{s0}(\xi_*) = 0$. Like in the previous case, the velocity and position of the singularity can in general be retrieved as $u_* = u_{s0}(\xi_*)$ and $x_* = \xi_* + t_*u_*$, respectively, and for symmetric distributions (as in figure 6a) we have that $u_* = 0$ and $x_* = \xi_*$.

Appendix E. Dictionary of initial conditions

Table 5 compiles the functional form of profiles $\Gamma_0(x) = \text{Im}[\psi_0(x)]$ and their Hilbert transforms $u_{s0}(x) = \text{Re}[\psi_0(x)] = \mathcal{H}[\Gamma_0(x)]$ used in §§ 4 and 5. In addition, the lower-analytic complex function $\psi_0(x + iy)$ that reduces to $\psi_0(x) = u_{s0}(x) + i\Gamma_0(x)$ on the real line ($y = 0$) is also provided. This function is required to compute exact solutions to (2.19) via the method of characteristics since the solution $\psi(x, t) = \psi_0(x - t\psi(x, t))$ involves evaluations of $\psi_0(z)$ at complex departure points z .

For spreading solutions, multiple pulses can be generated via linear combination $\psi_0(z) = \sum_{n=1}^N a_n \psi_{0,n}((z - c_n)/b_n)$ of N shifted and rescaled solutions $\psi_{0,n}$. The properties of the Hilbert transform (King 2009a) lead to simple expressions for the total mass $M_0 = \sum_{n=1}^N a_n b_n M_{0,n}$ and first moment $M_1 = \sum_{n=1}^N a_n b_n c_n M_{0,n}$, where $M_{0,n}$ is the mass of the n th pulse. For the double ($N = 2$) quartic pulse in figure 3(c), we fix $a_1 = a_2 = K$, $b_1 = 1/3$, $b_2 = 2/3$, $c_1 = -1/2$, $c_2 = 1$, with K such that $\max[\Gamma_0(x)] = 1$.

Dimple and hole profiles can be readily generated from a pulse $\psi_0^P(z)$ by defining $\psi_0^H(z) = i - \psi_0^P(z)$ for the dimple or hole. More complicated functional forms of $\psi_0(z)$ can be produced in a similar fashion. For instance, the asymmetric hole of figure 6(c), which has an expression that is too long to include in table 5, can be built using superposition and shifts of simpler profiles. If we label the half-Cauchy pulse of surfactant as $\psi_{0,A}(z)$, and the rectangular pulse as $\psi_{0,B}(z)$ (both in table 5), then the asymmetric hole can be generated as $\psi_0(z) = i - \psi_{0,A}(z - 1) - \psi_{0,B}(z)$.

REFERENCES

- AHMAD, J. & HANSEN, R.S. 1972 A simple quantitative treatment of the spreading of monolayers on thin liquid films. *J. Colloid Interface Sci.* **38** (3), 601–604.
- ALPERS, W. & HÜHNERFUSS, H. 1989 The damping of ocean waves by surface films: a new look at an old problem. *J. Geophys. Res.* **94** (C5), 6251–6265.
- BAKER, G.R., LI, X. & MORLET, A.C. 1996 Analytic structure of two 1D-transport equations with nonlocal fluxes. *Physica D* **91** (4), 349–375.
- BARENBLATT, G.I. 1996 *Scaling, Self-Similarity, and Intermediate Asymptotics*. Cambridge University Press.
- BICKEL, T. & DETCHEVERRY, F. 2022 Exact solutions for viscous Marangoni spreading. *Phys. Rev. E* **106** (4), 045107.
- BORGAS, M.S. & GROTBORG, J.B. 1988 Monolayer flow on a thin film. *J. Fluid Mech.* **193**, 151–170.
- BOTTE, V. & MANSUTTI, D. 2005 Numerical modelling of the Marangoni effects induced by plankton-generated surfactants. *J. Mar. Syst.* **57** (1), 55–69.
- BRENNER, M. & BERTOZZI, A. 1993 Spreading of droplets on a solid surface. *Phys. Rev. Lett.* **71** (4), 593–596.
- BRENNER, M.P., LISTER, J.R. & STONE, H.A. 1996 Pinching threads, singularities and the number 0.0304. *Phys. Fluids* **8** (11), 2827–2836.
- BREWARD, C.J.W. & HOWELL, P.D. 2002 The drainage of a foam lamella. *J. Fluid Mech.* **458**, 379–406.
- CANTAT, I., COHEN-ADDAD, S., ELIAS, F., GRANER, F., HÖHLER, R., PITOIS, O., ROUYER, F. & SAINT-JALMES, A. 2013 *Foams: Structure and Dynamics*. Oxford University Press.
- CHAE, D., CÓRDOBA, A., CÓRDOBA, D. & FONTELOS, M.A. 2005 Finite time singularities in a 1D model of the quasi-geostrophic equation. *Adv. Math.* **194** (1), 203–223.
- COX, D.A. 2012 *Galois Theory*. John Wiley & Sons.
- CROWDY, D.G. 2021a Exact solutions for the formation of stagnant caps of insoluble surfactant on a planar free surface. *J. Engng Maths* **131** (1), 10.
- CROWDY, D.G. 2021b Viscous Marangoni flow driven by insoluble surfactant and the complex Burgers equation. *SIAM J. Appl. Maths* **81** (6), 2526–2546.
- CROWDY, D.G., CURRAN, A.E. & PAPAGEORGIOU, D.T. 2023 Fast reaction of soluble surfactant can remobilize a stagnant cap. *J. Fluid Mech.* **969**, A8.
- CUENOT, B., MAGNAUDET, J. & SPENNATO, B. 1997 The effects of slightly soluble surfactants on the flow around a spherical bubble. *J. Fluid Mech.* **339**, 25–53.

Self-similarity in unbounded viscous Marangoni flows

- DAY, R.F., HINCH, E.J. & LISTER, J.R. 1998 Self-similar capillary pinchoff of an inviscid fluid. *Phys. Rev. Lett.* **80** (4), 704–707.
- EGGERS, J. 1993 Universal pinching of 3D axisymmetric free-surface flow. *Phys. Rev. Lett.* **71** (21), 3458–3460.
- EGGERS, J. 2000 Singularities in droplet pinching with vanishing viscosity. *SIAM J. Appl. Maths* **60** (6), 1997–2008.
- EGGERS, J. & FONTELOS, M.A. 2008 The role of self-similarity in singularities of partial differential equations. *Nonlinearity* **22** (1), R1.
- EGGERS, J. & FONTELOS, M.A. 2015 *Singularities: Formation, Structure and Propagation*. Cambridge University Press.
- EGGERS, J. & FONTELOS, M.A. 2020 Selection of singular solutions in non-local transport equations. *Nonlinearity* **33** (1), 325.
- ERININ, M.A., LIU, C., LIU, X., MOSTERT, W., DEIKE, L. & DUNCAN, J.H. 2023 The effects of surfactants on plunging breakers. *J. Fluid Mech.* **972**, R5.
- FRUMKIN, A.N. & LEVICH, V.G. 1947 On surfactants and interfacial motion. *Zh. Fiz. Khim.* **21**, 1183–1204.
- GAVER, D.P. & GROTBORG, J.B. 1990 The dynamics of a localized surfactant on a thin film. *J. Fluid Mech.* **213**, 127–148.
- GAVER, D.P. & GROTBORG, J.B. 1992 Droplet spreading on a thin viscous film. *J. Fluid Mech.* **235**, 399–414.
- DE GENNES, P.-G., BROCHARD-WYART, F. & QUÉRÉ, D. 2004 *Capillarity and Wetting Phenomena*. Springer.
- GIGA, Y. & KOHN, R.V. 1985 Asymptotically self-similar blow-up of semilinear heat equations. *Commun. Pure Appl. Maths* **38** (3), 297–319.
- GIGA, Y. & KOHN, R.V. 1987 Characterizing blowup using similarity variables. *Indiana Univ. Math. J.* **36** (1), 1–40.
- GRATTON, J. & MINOTTI, F. 1990 Self-similar viscous gravity currents: phase-plane formalism. *J. Fluid Mech.* **210**, 155–182.
- GRIFFITH, R.M. 1962 The effect of surfactants on the terminal velocity of drops and bubbles. *Chem. Engng Sci.* **17** (12), 1057–1070.
- GROTBORG, J.B., HALPERN, D. & JENSEN, O.E. 1995 Interaction of exogenous and endogenous surfactant: spreading-rate effects. *J. Appl. Physiol.* **78** (2), 750–756.
- DE LA HOZ, F. & FONTELOS, M.A. 2008 The structure of singularities in nonlocal transport equations. *J. Phys. A: Math. Theor.* **41** (18), 185204.
- HUPPERT, H.E. 1982 The propagation of two-dimensional and axisymmetric viscous gravity currents over a rigid horizontal surface. *J. Fluid Mech.* **121**, 43–58.
- JENSEN, O.E. 1994 Self-similar, surfactant-driven flows. *Phys. Fluids* **6** (3), 1084–1094.
- JENSEN, O.E. 1995 The spreading of insoluble surfactant at the free surface of a deep fluid layer. *J. Fluid Mech.* **293**, 349–378.
- JENSEN, O.E. & GROTBORG, J.B. 1992 Insoluble surfactant spreading on a thin viscous film: shock evolution and film rupture. *J. Fluid Mech.* **240**, 259–288.
- JENSEN, O.E. & GROTBORG, J.B. 1993 The spreading of heat or soluble surfactant along a thin liquid film. *Phys. Fluids A: Fluid Dyn.* **5** (1), 58–68.
- KANEELIL, P.R., PAHLAVAN, A.A., XUE, N. & STONE, H.A. 2022 Three-dimensional self-similarity of coalescing viscous drops in the thin-film regime. *Phys. Rev. Lett.* **129** (14), 144501.
- KING, F.W. 2009a *Hilbert Transforms*, vol. 1. Cambridge University Press.
- KING, F.W. 2009b *Hilbert Transforms*, vol. 2. Cambridge University Press.
- LEAL, L.G. 2007 *Advanced Transport Phenomena: Fluid Mechanics and Convective Transport Processes*. Cambridge University Press.
- LISTER, J.R. & KERR, R.C. 1989 The propagation of two-dimensional and axisymmetric viscous gravity currents at a fluid interface. *J. Fluid Mech.* **203**, 215–249.
- LIU, X. & DUNCAN, J.H. 2003 The effects of surfactants on spilling breaking waves. *Nature* **421** (6922), 520–523.
- LUCASSEN, J. & VAN DEN TEMPEL, M. 1972 Dynamic measurements of dilational properties of a liquid interface. *Chem. Engng Sci.* **27** (6), 1283–1291.
- MANIKANTAN, H. & SQUIRES, T.M. 2020 Surfactant dynamics: hidden variables controlling fluid flows. *J. Fluid Mech.* **892**, P1.
- MATAR, O.K. & CRASTER, R.V. 2009 Dynamics of surfactant-assisted spreading. *Soft Matt.* **5** (20), 3801–3809.
- MORLET, A.C. 1998 Further properties of a continuum of model equations with globally defined flux. *J. Math. Anal. Appl.* **221** (1), 132–160.

- OLVER, F.W.J., OZIER, D.W., BOISVERT, R.F. & CLARK, C.W. (Eds) 2010 *NIST Handbook of Mathematical Functions*. Cambridge University Press.
- OLVER, P.J. 2014 *Introduction to Partial Differential Equations*. Springer.
- PALAPARTHI, R., PAPAGEORGIOU, D.T. & MALDARELLI, C. 2006 Theory and experiments on the stagnant cap regime in the motion of spherical surfactant-laden bubbles. *J. Fluid Mech.* **559**, 1–44.
- PARK, C.-W. 1991 Effects of insoluble surfactants on dip coating. *J. Colloid Interface Sci.* **146** (2), 382–394.
- PEAUDECERF, F.J., LANDEL, J.R., GOLDSTEIN, R.E. & LUZZATTO-FEGIZ, P. 2017 Traces of surfactants can severely limit the drag reduction of superhydrophobic surfaces. *Proc. Natl Acad. Sci. USA* **114** (28), 7254–7259.
- POZRIKIDIS, C. 1992 *Boundary Integral and Singularity Methods for Linearized Viscous Flow*. Cambridge University Press.
- QUÉRÉ, D. 1999 Fluid coating on a fiber. *Annu. Rev. Fluid Mech.* **31** (1), 347–384.
- SADHAL, S.S. & JOHNSON, R.E. 1983 Stokes flow past bubbles and drops partially coated with thin films. Part 1. Stagnant cap of surfactant film – exact solution. *J. Fluid Mech.* **126**, 237–250.
- SCHECHTER, R.S. & FARLEY, R.W. 1963 Interfacial tension gradients and droplet behavior. *Can. J. Chem. Engng* **41** (3), 103–107.
- SCRIVEN, L.E. & STERNLING, C.V. 1960 The Marangoni effects. *Nature* **187** (4733), 186–188.
- SLIM, A.C. & HUPPERT, H.E. 2004 Self-similar solutions of the axisymmetric shallow-water equations governing converging inviscid gravity currents. *J. Fluid Mech.* **506**, 331–355.
- SONG, D., SONG, B., HU, H., DU, X., DU, P., CHOI, C.-H. & ROTHSTEIN, J.P. 2018 Effect of a surface tension gradient on the slip flow along a superhydrophobic air–water interface. *Phys. Rev. Fluids* **3** (3), 033303.
- STROGATZ, S.H. 2018 *Nonlinear Dynamics and Chaos: With Applications to Physics, Biology, Chemistry, and Engineering*. CRC Press.
- TEMPRANO-COLETO, F., SMITH, S.M., PEAUDECERF, F.J., LANDEL, J.R., GIBOU, F. & LUZZATTO-FEGIZ, P. 2023 A single parameter can predict surfactant impairment of superhydrophobic drag reduction. *Proc. Natl Acad. Sci. USA* **120** (3), e2211092120.
- THESS, A. 1996 Stokes flow at infinite Marangoni number: exact solutions for the spreading and collapse of a surfactant. *Phys. Scr.* **1996** (T67), 96.
- THESS, A., SPIRN, D. & JÜTTNER, B. 1995 Viscous flow at infinite Marangoni number. *Phys. Rev. Lett.* **75** (25), 4614–4617.
- THESS, A., SPIRN, D. & JÜTTNER, B. 1997 A two-dimensional model for slow convection at infinite Marangoni number. *J. Fluid Mech.* **331**, 283–312.
- TRINSCHKE, S., JOHN, K. & THIELE, U. 2018 Modelling of surfactant-driven front instabilities in spreading bacterial colonies. *Soft Matt.* **14** (22), 4464–4476.
- WANG, Y., PAPAGEORGIOU, D.T. & MALDARELLI, C. 1999 Increased mobility of a surfactant-retarded bubble at high bulk concentrations. *J. Fluid Mech.* **390**, 251–270.
- WASSERMAN, M.L. & SLATTERY, J.C. 1969 Creeping flow past a fluid globule when a trace of surfactant is present. *AIChE J.* **15** (4), 533–547.
- WU, K., DUPRAT, C. & STONE, H.A. 2024 Capillary rise in sharp corners: not quite universal. *J. Fluid Mech.* **978**, A26.
- ZHENG, Z., FONTELOS, M.A., SHIN, S. & STONE, H.A. 2018 Universality in the nonlinear leveling of capillary films. *Phys. Rev. Fluids* **3** (3), 032001.
- ZHONG, L., KETELAAR, C.F., BRAUN, R.J., BEGLEY, C.G. & KING-SMITH, P.E. 2019 Mathematical modelling of glob-driven tear film breakup. *Math. Med. Biol.* **36** (1), 55–91.